Delft University of Technology

Numerical prediction on the fatigue debonding behaviour in a complex bi-material interface
A case study on wrapped composite joints

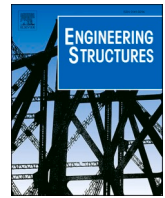Feng, Weikang; Egilsson, Sigurdur; Wolters, Mees; Pavlovic, Marko

Important note
To cite this publication, please use the final published version (if applicable).
Please check the document version above.

Numerical prediction on the fatigue debonding behaviour in a complex bi-material interface: A case study on wrapped composite joints

Weikang Feng [a], Sigurdur Egilsson [a], Mees Wolters [b], Marko Pavlovic [a],*

[a] *Faculty of Civil Engineering and Geoscience, Delft University of Technology, Delft, the Netherlands*
[b] *Tree Composites B.V., Delft, the Netherlands*

ARTICLE INFO

ABSTRACT

Debonding is one of the most critical failure modes for bonded joints under fatigue loads. Numerical prediction on the fatigue debonding behaviour of bonded interfaces with complex geometry still remains a problem. This paper proposes a numerical methodology based on fracture mechanics to predict crack growth in a complex bi-material interface and illustrates the prediction procedure by a case study on wrapped composite joints. Interface coupon tests provide the fatigue crack growth properties at the composite-to-steel interface used as inputs for finite element (FE) modelling. The FE model is calibrated against fatigue tests of small scale wrapped composite joints with different steel surface roughness subject to different load levels. A sensitivity analysis is conducted to investigate the influence of key modelling parameters. The calibrated model is validated against fatigue tests on upscaled joints. Good agreements are shown between the test and modelling results in terms of crack growth and stiffness degradation, demonstrating the potential of the proposed numerical methodology for predicting fatigue debonding behaviour of complex bi-material interfaces.

1. Introduction

Bonded joints have been widely used in engineering structures due to their design flexibility, lower stress concentration, and the unnecessity of drilling holes in connected elements [1]. One typical application of such joints is connecting composite materials and steel elements for strengthening existing steel structures or joining elements in new structures [2]. The use of composite materials makes the whole steel structure have higher strength, lower self-weight, better fatigue and corrosion resistance, et al., especially for offshore steel structures. Wrapped composite joint, proposed by the authors [3–5], connects steel circular hollow sections (CHS) in jacket support structures of offshore wind turbine towers through bonded composite wrap. The forces among different CHS elements are transferred through the bonded interface instead of the welds, resulting in better fatigue performance of the wrapped composite joints compared to traditional welded ones. However, wrapped composite joints still suffer debonding failure at the composite-to-steel interface under cyclic loading [6]. The cumbersome fatigue testing and crack monitoring technique on the wrapped composite joints makes it difficult to consistently predict the fatigue life of the joints through experimental work. Therefore, a numerical method

for predicting fatigue crack growth at such complex 3D bonded interfaces needs to be developed.

In literature, roughly three categories of methods have been developed for predicting fatigue delamination within composite layers or debonding between dissimilar adherends [7]: 1) stress/strain methods; 2) damage mechanics-based methods and 3) fracture mechanics-based methods. The stress/strain method is usually applicable to static delamination / debonding problems. It is commonly used to predict the fatigue life instead of the fatigue crack growth process [8,9]. Limited work has also been done to correlate the stress or strain in the material to the fatigue crack growth rates [10,11], which successfully predicted the test results. However, the complex stress fields and singularity arising at the bonded interface, especially at the bi-material interface, makes the application of stress / strain based methods still limited.

The damage mechanics-based method adopts cohesive zone models (CZMs) [12]. It is based on a traction-separation law defined at the interface (or interface elements), where the key inputs include the initial stiffness, the maximum tractions and the fracture toughness. Under fatigue loading, the traction-separation law is modified by degrading the stiffness, strength as well as the fracture energy as a function of load cycles [13]. While showing the ability to simulate the damage

---

* Corresponding author.
E-mail address: M.Pavlovic@tudelft.nl (M. Pavlovic).

accumulation process, adequately accurate modelling results and sufficient computation efficiency [14–16], few disadvantages hinder the application of CZM. For instance, some of the parameters in the traction-separation law are difficult to be characterised through experiments, while other parameters need to be fitted. The complex implementation of the fatigue damage evolution law limits the use of CZM in existing commercial finite element (FE) software.

A widely used numerical method for predicting fatigue crack propagation in composite materials is based on fracture mechanics, where the crack growth rates are linked to the strain energy release rates (SERR) at the crack tip through fatigue crack growth (FCG) curves or Paris curves [17]. The FE method is usually utilised for calculating the SERR values and one widely used method is the virtual crack closure technique (VCCT) [18]. Knowing the SERR values, the crack growth can be predicted by integrating FCG curves or Paris curves. In practice, the number of cycles corresponding to a certain crack length a_f can be calculated numerically using the incremental form of $N_f = \sum_{i=1}^{n} \frac{\Delta a}{F(G_i^*)}$, where a_f is divided into n small increments Δa, F is the formula of FCG or Paris curves adopting different forms, and G_i^* is the crack driving force with different forms of SERR [19]. In Quaresimin and Ricotta's work [20,21], SERR values of various mixed fracture modes at the crack tips of single lap joints are extracted from the FE model, expressed as a function of crack length and applied stress level. The number of cycles for crack propagation within the joint is calculated by integration of Paris curves. Another option in the FE software, e.g. in Abaqus [22], to model the cyclic response of the structure directly is to combine the VCCT with direct cyclic analysis. Pirondi et al. [23] applied the direct cyclic analysis to predict the crack growth in DCB, ENF and SLJ joints where different mode mixities existed. The VCCT model gave rather good agreement with the test results with regard to crack length vs. number of cycles and SERR vs. crack length. However, this procedure requires lots of computational time due to iterations needed for the convergence of ΔG value. Using the implicit solver, this analysis is even incapable of running properly for bonded joints with a complex geometry and multiple contact interactions. The fixed Paris-like crack growth law in the analysis also makes this method not versatile enough for different fracture conditions. To overcome the problems, Martulli and Bernasconi [24] proposed the sequential static fatigue (SSF) analysis for composite delamination growth. It is a 3D VCCT-based algorithm, which can reduce the computational time compared to the direct cyclic analysis by launching a series of static simulations. Case studies using SSF on different types of specimens showed good agreements with test results. Another case of utilizing VCCT in simulating fatigue delamination in composites is from Russo et al. [25,26]. In their studies a robust numerical methodology based on Smart-Time XB procedure was developed to simulate delamination in coupon and complex joints, where load step size and mesh size independencies of VCCT is overcome.

While having been used in various fatigue crack growth scenarios, VCCT still lacks implementation in simulating fatigue debonding in real engineering structures, especially for bi-material cases. The geometry of bonded joints in real engineering is usually three dimensional and complex, while existed literature only focused on simple flat joints. Moreover, multiple debonding cracks usually develop simultaneously in reality. The growth of one crack may influence that of the other and vice versa. Seldom of existed study considered this phenomenon. This study extends the use of VCCT to simulate fatigue debonding in a complex bi-material interface, the composite-to-steel interface of wrapped composite joints, using the more robust explicit solver. In this procedure, a series of static simulations on the joints with predefined cracks on the chord and braces are run to extract SERR values at the crack tips. The number of cycles needed for crack growth is calculated using a post-processing script, where the interaction of debonding on the chord and braces is considered. Fatigue tests on the interface coupons, 4-point end notched flexure (4ENF) specimens, provide fatigue crack growth properties at the composite-to-steel interface, which serve as inputs for

the analysis at the joint level. FE simulations on the joint are conducted using the proposed method, with key modelling parameters calibrated against small scale joints with different steel roughness, tested under different load levels. Finally, the calibrated FE simulation is applied to upscaled joints to validate the potential application of the proposed methodology in real engineering scenarios.

2. Experimental work

2.1. Interface coupon tests

Fatigue crack growth (FCG) properties at the interface coupon level, i.e. at the composite-to-steel interface, are characterised in this section. Usually multiple fracture modes may exist in complex interfaces (e.g. in wrapped composite joints) during the failure process, including mode I (resulting from peel stresses), mode II (resulting from in-plane shear stresses) and mixed mode fractures. As will be revealed by the finite element analysis in the following sections, the mode II fracture is the dominant fracture mode in the tensile loading case of the wrapped composite joint. Therefore, the mode II FCG property at the composite-to-steel interface is characterised. Meanwhile, the bond quality of the joint highly relies on the surface preparation, e.g. surface roughness, of the steel members. In Ref. [27], the fracture toughness (G_{IIc}) and FCG properties of the composite-to-steel interface were characterized for different roughness levels. The procedure is illustrated in Fig. 1. Fracture toughness of the bonded interface was obtained through quasi-static 4ENF tests as shown in Fig. 1(a), based on which the relationship between fracture toughness and roughness parameter S_q was obtained in Fig. 1(b). The fracture toughness was obtained through finite element models using virtual crack closure technique (VCCT) to consider the friction effect at the interface. Details were given in Ref. [27] and will not be expanded here.

The FCG properties were characterized through fatigue 4ENF tests. The relationships between crack growth rate, da/dN, and the driving force, mode II strain energy release rate (SERR) range (ΔG_{II}), are fitted by the classical power function in Eq. (1) for different roughness series as shown in Fig. 1(c) i. By fixing the slope m of the Paris curves, the relationship of the intercept C and the roughness parameter can be obtained and fitted in Fig. 1(d). However, the simple power function has the limitation of considering the influence of threshold strain energy release rate (G_{IIth}) and the fracture toughness. This limitation may lead to overestimation of the crack growth rates near the threshold and underestimation near the fracture toughness, respectively. A total life FCG model was proposed by Martin and Murri [17] as expressed in Eq. (2) to avoid this issue. This model covers all the three stages of FCG curve: the subcritical region around G_{IIth}, the power function controlled region and the critical region close to G_{IIc}. One example of data fitting by the total life FCG model for different roughness series is illustrated in Fig. 1(c) ii. In Eq. (2), G_{IIth} can be obtained by the crack growth onset tests [28] or by visual observation of the experimentally obtained FCG curves [29]. The exponents D_1 and D_2 determine the curvature of the FCG curve near G_{IIth} and G_{IIc} and can be obtained by fitting the test data.

$$da/dN = C(\Delta G_{II})^m \tag{1}$$

$$da/dN = C(\Delta G_{II})^m \frac{\left[1 - \left(\frac{G_{IIth}}{\Delta G_{II}}\right)^{D_1}\right]}{\left[1 - \left(\frac{\Delta G_{II}}{G_{IIc}}\right)^{D_2}\right]} \tag{2}$$

However, it is difficult to determine the threshold G_{IIth} and curvature exponents D_1 and D_2 by fitting the test data directly in the current study, since no obvious threshold behaviour is observed. According to the literature [17,22,30–32], G_{th} can be 1 % to over 20 % of G_c, depending on the materials, stress ratio etc. In the current study, the minimum SERR values of different roughness series, which are obviously above
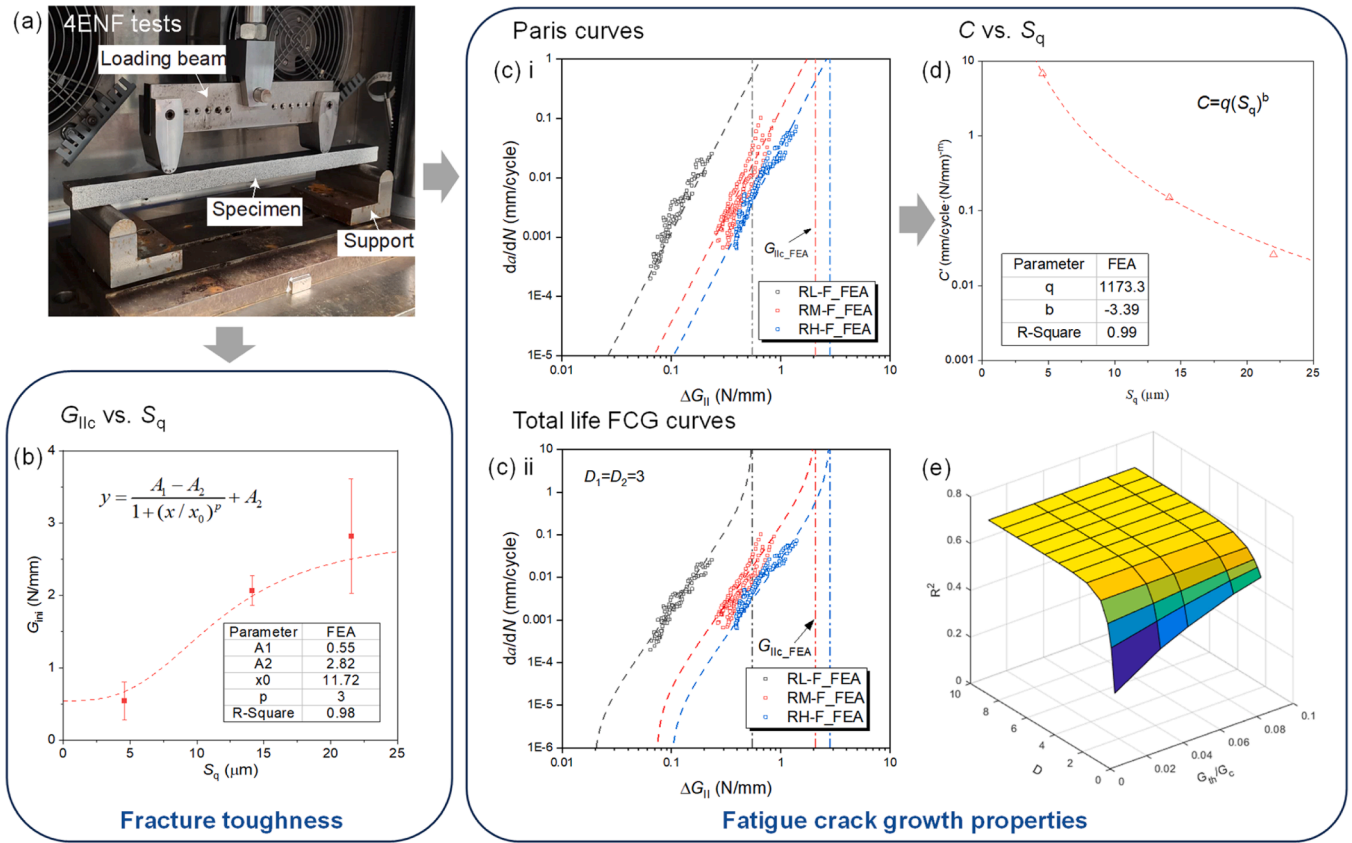
Fig. 1. Interface coupon tests for obtaining fracture toughness and FCG properties at the composite-to-steel interface as inputs for numerical prediction [27].

G_{IIth}, can be 9 %−13 % of G_{IIc}, indicating that the ratio between G_{th} and G_c cannot be larger than 9 %. A sensitivity study is conducted on the threshold ratio G_{IIth}/G_{IIc} in the range of 1 %−9 % and curvature exponent D_1 (D_2) of different magnitudes to evaluate the fitting quality, in order to determine the reasonable values of these two parameters. It is assumed in the current study that $D_1 = D_2 = D$, namely the FCG curve is assumed to be centrally symmetric about its midpoint.

The interactive influence of threshold ratio G_{IIth}/G_{IIc} and curvature exponent D on the fitting quality, R^2, is shown in Fig. 1(e). The results show that R^2 improves as G_{IIth}/G_{IIc} and D increase but converges to a fixed value when D is above 3 regardless of the value of G_{IIth}/G_{IIc}. This fixed value, 0.67, is approximately the same as that obtained when fitting by the power function, since the total life FCG model overlaps well with the power function in the range of test data when $D \geq 3$. With the preliminary possible range obtained through the sensitivity analysis ($D \geq 3$ % and 1 % $\leq G_{IIth}/G_{IIc} \leq 9$ %), the optimal combination of G_{IIth}/G_{IIc} and D will be further determined through model calibration against test results on small scale wrapped composite joints in Section 4.

2.2. Small scale joint tests for model calibration

Fatigue tests on small scale wrapped composite joints are used to calibrate the finite element (FE) model which will be introduced in the following sections. Geometry and dimensions of the specimens, as well as the test set-up, are shown in Fig. 2. These specimens are produced by joining two brace members made of circular hollow section (CHS) to the chord member, with the intersection angle of 45°, by glass fibre composite wrapping. Surfaces of steel tubes were grit blasted before wrapping and chemically degreased to ensure enough bonding strength between composite laminates and steel tubes. Details about the production of the specimens, composite materials, test set-up, strain measurement and debonding crack growth monitoring can be found in
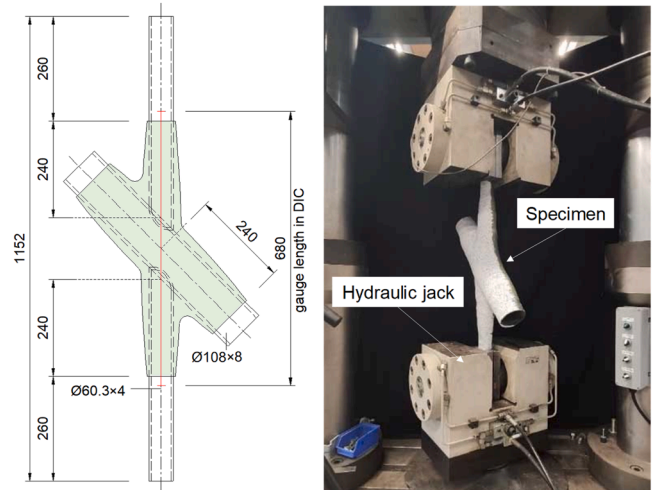

Fig. 2. Specimen dimensions and test set-up of small scale joints.

Ref. [3,33] and will not be expanded here. Test matrix is summarised in Table 1. A total of 6 specimens with different steel surface roughness are tested under different load levels for model calibration. Surface roughness (represented by the root mean square height S_q) of the steel tubes were measured by a profilemeter and the average values measured at multiple locations on each joint, as introduced in Ref. [3], are listed in the table. The specimens are loaded under force control with the frequency of 4 Hz and R-ratio of 0.1, up to 30 % (110 kN) and 50 % (165 kN) of the joints' ultimate loads [4], respectively.

Table 1
Test matrix for model calibration and validation.

Function	Series	Specimens	S_q (μm)	Load range (kN)	Frequency (Hz)
Model calibration	(a)	cX45-Ss-T_F2.1/2	16.78	10−110	
	(b)	cX45-Ss-T_F3.1/2		15−165	4
	(c)	cX45-Ss-T_F4.1/2	10.98	15−165	
Model validation	(d)	cX45-Us-T_F1.1/2/3	22.07	30−330	1

2.3. Upscaled joint tests for model validation

After being calibrated through small scale wrapped composite joint tests, the FE model is then validated against tests on upscaled joints, which are closer to the full scale application of the joints in jacket support structures. Geometry and dimensions of the upscaled joint are shown in Fig. 3. Dimensions of the chord and braces are Ø273 × 10 mm and Ø168 × 12.5 mm, respectively. The wrapping length on the brace is 4 times the brace diameter, which is the same ratio as used for the small scale joint. The maximum wrapping thickness at the root of the joint is around 50 mm. Ear plates are welded at ends of the steel tubes for the load application. The full penetration butt weld details are designed carefully to avoid possible premature failure. A hole is drilled at the end of the plate to ensure the welding quality. Materials and production of the specimens are the same as those for small scale joints.

As shown in Fig. 3, a self-equilibrium custom modular frame is built and equipped with the synchronized hydraulic jack on the top. The specimen is connected with the hydraulic jack through the ear plate. A pin shaft is used for the connection so that no bending moment is transferred at the loading ends. The identical 3D DIC system as utilized for the small-scale test is employed here to observe the deformations and displacements of the specimens throughout the test. To enhance the
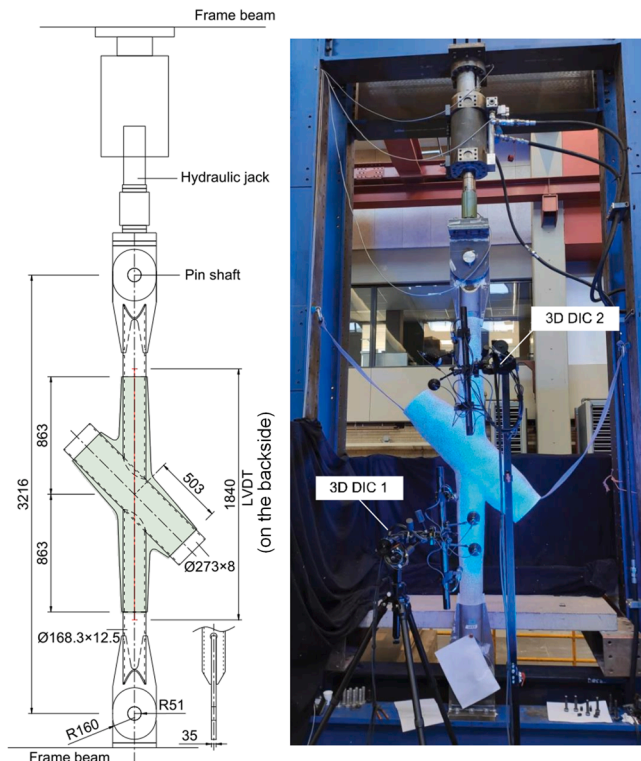
measuring accuracy of the DIC system and account for the measuring volume, two distinct DIC setups are established, each dedicated to one side of the chord-to-brace connection. The two DIC systems are controlled synchronously, taking photos at the maximum and minimum loads every 10000 cycles. An LVDT system is installed on the backside of the specimen to accurately measure its deformation, enabling the calculation of the global stiffness of the joint. The measuring length is 1840 mm as shown in this figure, encompassing not only the composite wrap but also a portion of the steel tube.

3 identical specimens with S_q = 22.07 μm are used for model validation as listed in Table 1. The tension-tension cyclic load is applied by force control with the range of 30–330kN, approximately 30 % of its static resistance. The bottom of the specimen is fixed during cyclic loading while the force is applied through the hydraulic jack on the top. The loading frequency is lowered down to 1 Hz to ensure the stability of the loading system.

3. Modelling strategy

3.1. Model set-up

3.1.1. Geometry and boundary conditions

Geometry of the small scale X45 joint FE model in ABAQUS software is shown in Fig. 4. Due to the symmetric geometry, only half of the joint is modelled to reduce the computational time. The geometry of steel tubes follows the design drawings of the specimen, while the dimensions of the composite part (thicknesses on flat parts and corners) are determined with the help of 3D scanning of the specimen. The composite part is modelled with 3 layers as has been applied during the production process. Surfaces representing the end cross sections of the braces are coupled to reference points, RP1 and RP2, as shown in the figure. All degrees of freedom except for the U2 (y) direction are constrained for the reference points to replicate the fixation constraints at the tube ends due to clamping in the physical test. The symmetric tensile load is applied by vertical displacement on both RP1 and RP2. Symmetric boundary conditions are applied in the middle (cut) plane.

3.1.2. Analyses method

Due to the complexity and nonlinearity of deformations, interactions and materials in the model, the analysis is performed using the dynamic explicit solver in ABAQUS. To mitigate inertia effects in quasi-static
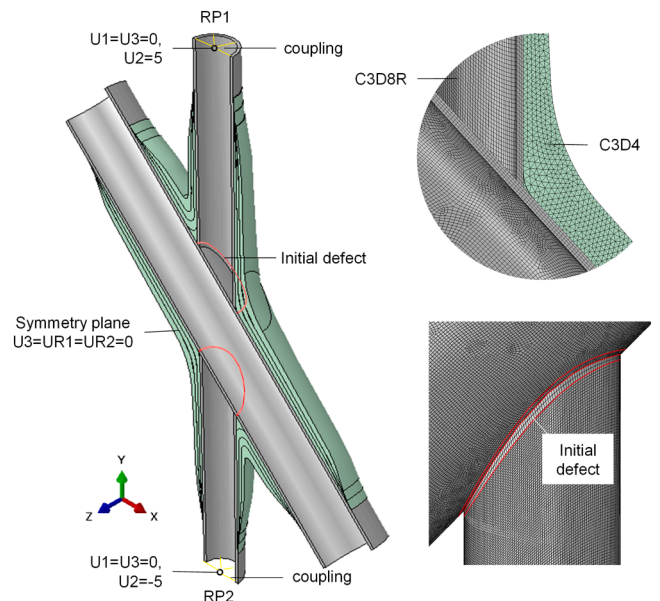

Fig. 3. Specimen dimensions and test set-up of upscaled joints.

Fig. 4. Boundary conditions and mesh topology of the FE model.

explicit dynamic analysis, the displacement is applied using a smooth step amplitude curve. The time period of the analysis was chosen similar to its real time period (e.g. 300 s for monotonic loading). But the quasi-static analysis is sped up by employing non-uniform, semi-automatic mass scaling in the explicit solver. The desired time increment for integration is set to be 0.005 s, which is small enough to match the input and output forces as suggested by [34].

3.1.3. Materials

Material of the composite wrap is considered as transversely isotropic. The elastic constants are obtained through standard material tests on the GFRP laminate ($E_1 = E_2$, G_{12} and υ_{12}) [3] and based on classical laminate theory for data not obtained directly by tests (E_3, G_{13} = G_{23}, υ_{13} = υ_{23}) as shown in Table 2. Further information on plasticity and material damage can be found in [34]. For steel parts, the isotropic elastic properties are listed in Table 2. Nominal yield and ultimate stress (S355, f_y = 355 MPa, f_u = 510 MPa) in combination with isotropic hardening are used to model the plastic behaviour.

3.1.4. Interactions

Tie constraint is applied between different wrapping layers considering the fact that limited interlaminar damage was found in the wrap. As for the composite-to-steel interface, VCCT is utilized to simulate the crack propagation at the interface in the static model and calculate the SERR at the crack tips for fatigue analysis. Initial defects of 2 mm (2-element size) are introduced on the chord and braces respectively at the intersection of the connected steel members as depicted in Fig. 4 to initiate the crack propagation. The nodes in front of the crack tip from both steel and composite parts are coupled and will debond after the fracture criterion, $G_T \geq G_{eqC}$, is met. For the Benzeggagh–Kenane (BK) law [35] used in this study, G_T represents the total SERR, i.e G_T = G_I + G_{II} + G_{III}. G_{eqC} is the equivalent critical SERR, which is defined by:

$$G_{eqC} = G_{IC} + \left(G_{IIC} - G_{IC} \right) \left(\frac{G_{II} + G_{III}}{G_T} \right)^{\eta} \tag{3}$$

where G_{IC} and G_{IIC} are the critical mode I and mode II SERRs, and $\eta = 1.8$. Considering the limitations of VCCT in defining the initiation and propagation values of SERR, the critical SERR values obtained by the standard DCB and ENF test cannot be directly used as the inputs [36]. A friction behaviour in combination with calibrated critical SERR values are defined at the interface as listed in Table 3. The friction coefficient $\mu = 0.5$ is measured by the tribometer as introduced in Ref. [27]. The critical SERR values are tuned between the initiation value and propagation value which are obtained in [34] until achieving a satisfactory alignment with the force-displacement curves. The mode I critical SERR value is adjusted proportionally to the mode II value during the tuning process.

In modelling of fatigue behaviour, the critical SERR values are intentionally set to a sufficiently high level (e.g. 100 N/mm) to prevent crack propagation, such that SERR values can be calculated at a specific stationary crack tip.

3.1.5. Finite element mesh

Linear, hexahedral solid elements, C3D8R, with reduced integration are used for the brace and chord steel members. Linear tetrahedron elements, C3D4, are used for the composite wrap due to its complex

Table 2
Elastic material properties.

Material name	Elastic constants [GPa]	Poisson's ratio
Composite wrap (GFRP)	$E_1 = E_2 = 12.0$, $E_3 = 6.6$, $G_{12} = 3.1$, $G_{13} = G_{23} = 2.5$	$\upsilon_{12} = 0.15$, $\upsilon_{13} = \upsilon_{23}$ = 0.3
Steel members (S355)	$E_1 = 210$	$\upsilon = 0.3$

geometry. The composite parts are modelled as 3 non-uniformly thick laminates by 3D solid elements instead of multiple plies by shell elements since the delamination is insignificant as inspected after the fatigue tests [3]. Since the SERR values calculated by the VCCT are sensitive to the mesh size [18], a sensitivity study on the global mesh size is conducted. The results in Fig. 5 show that the SERR values converged within the investigated mesh size range of 0.5–2 mm. Taking into account both accuracy and computational efficiency, a global mesh size of 1 mm is chosen for the subsequent analysis.

3.2. Preliminary model validation against quasi-static tests

The FE model is validated against the results of quasi-static tests in terms of force-displacement responses and strain distribution on the composite wrap in the section. Force-displacement curves from the VCCT-based FE model with and without friction defined at the interface are plotted and compared with test results presented in Ref. [34] in Fig. 6. The figure shows that the VCCT-based model with friction matches well with the test results in terms of curve shapes, initial stiffness and ultimate resistance. On the contrary, FE model without friction exhibits an abrupt failure after reaching the elastic limit, i.e. after the fracture criterion Eq. (3) is met. This contrast proves that friction can effectively simulate the residual interaction (friction, fibre bridging, etc.) behaviour at the interface after fracture.

A significant mismatch between the VCCT-based FEA result and test results is observed in the elastic limit as indicated in Fig. 6, where the FEA tends to overestimate the test results. However, the mismatch is not observed in the CZM-based model as in Ref. [34]. This is again due to the limitation of VCCT in simulating the fracture process zone. The elastic limit in the force-displacement curve corresponds to onset value of SERR in the CZM [34], which is lower than the tuned critical SERR values in the VCCT model. A sawtooth behaviour is also evident in the VCCT-based results, wherein drops of the force are associated with node releases every time the new crack front forms [18]. This nonlinear and sawtooth behaviour is above the target maximum force during the fatigue test thus will not influence the SERR calculation for the following analysis on fatigue behaviour.

The FE model is further validated by comparing strain distributions on the surface of the FE model with DIC results of specimen cX45-Ss-T_S3.1&2 at different loading stages as shown in Fig. 7 (165 kN, stage (a) in Fig. 6 corresponding to the maximum load in cyclic loading) and Fig. 8 (300 kN, stage (b) in Fig. 6 where a certain level of debonding has happened on the chord and braces). According to these two figures, the contour plots of major strains on the surface and extracted along the path from the FE model resembles well with those from DIC analysis. The strains concentrate at the brace-to-chord corners and decrease gradually towards the end of brace.

3.3. The stationary crack growth method

The methodology for predicting crack growth and stiffness degradation of the joints, called the stationary crack growth method, is introduced in this section. The target of this method is to calculate the number of cycles needed for certain predefined crack patterns and lengths. The following assumptions are made for this method for simplification and due to limitations of the modelling technique (e.g. the debonding on the top and bottom braces is different due to different surface conditions of the steel tubes [6], which cannot be considered in the numerical model):

1) Debonding at the composite-to-steel interface is the only failure mode under cyclic loading, with all the materials remaining elastic;
2) The debonding patterns under cyclic loading are consistent with those observed in quasi-static loading when composite materials stay in elasticity. But the relationship between the debonding crack length on the chord and braces may be different;

Table 3
Interaction property parameters.

Parameter	Mode I				Mode II			
	G_{Ic} (N/mm)	G_{Iini}* (N/mm)	G_{Iprop}* (N/mm)	$(G_{Ic} - G_{Iini})/$ $(G_{Ipro} - G_{Iini})$**	G_{IIc} (N/mm)	G_{IIini}* (N/mm)	G_{IIprop}* (N/mm)	$(G_{IIc} - G_{IIini})/$ $(G_{IIpro} - G_{IIini})$**
Values	1.02	0.3	1.2	77 %	1.34	0.45	1.6	77 %

* Obtained from Ref. [34]
** The critical values are tuned between the initiation value and propagation value. This percentage (weight) expresses the contribution of initiation and propagation SERR to the fracture criterion.
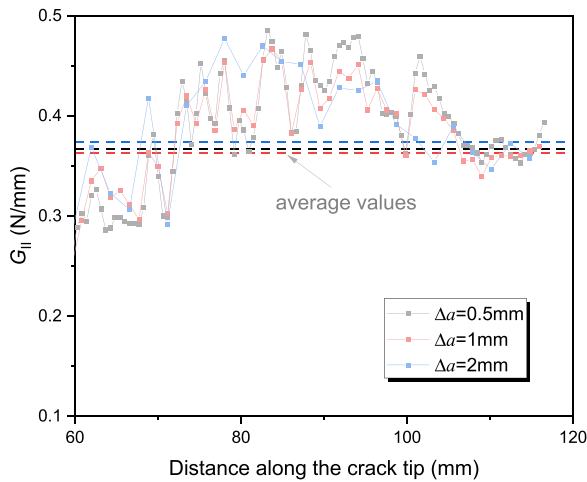
Fig. 5. Mesh sensitivity analysis.
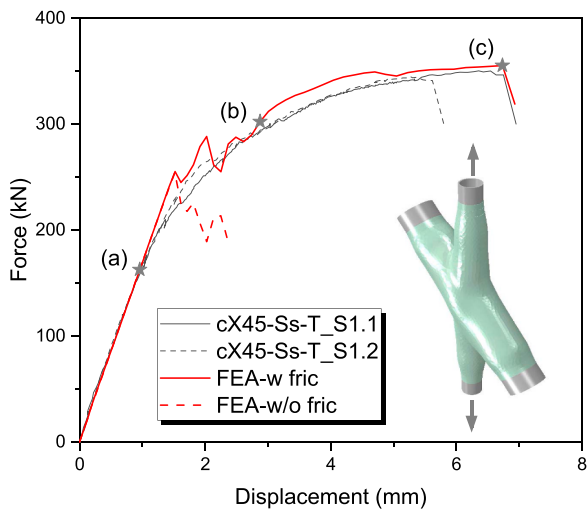
Fig. 6. Comparison of force-displacement responses between FEA and test results.

3) Debonding on the top and bottom sides of the joints are centrally symmetric about the origin;
4) Definitions of crack lengths on the chord and braces are shown in Fig. 9. L_b is defined as the distance from the obtuse corner to the midpoint of the crack tip along the brace's axis, while L_c is defined as length of the arc perpendicular to the chord's axis, starting from the midpoint of the intersection between the brace and chord to the crack tip.

Based on the assumptions above, the fatigue debonding behaviour of the wrapped composite joints is predicted using the procedure outlined in the flowchart in Fig. 10. This procedure includes the finite element

modelling, followed by a post-processing script for the cycle calculation. Detailed explanations and intermediate results obtained from each step will be discussed in the following part.

Step1: obtain crack patterns from static model.

The debonding crack patterns developed under cyclic loading are obtained by loading the model monotonically in the first step. It should be noted that materials are assumed to remain elastic in cyclic loading since the composite wrap is thick enough and the maximum force (e.g. 165 kN for small scale joints) is below the elastic limit. In this case, damages only evolve at the interface, which is different from the static model where damages evolve both at the interface and within materials. This discrepancy in the damage evolution may result in variations in the debonding patterns under monotonic and cyclic loadings. The static model is re-run with all the material properties set to be elastic to eliminate the influence of this discrepancy.

Debonding procedure of the elastic model under monotonic loading is shown in Fig. 11. The bond states (BDSTAT) at different loading stages are shown in this figure, with the blue colour (BDSTAT=0) represents fully debonded region, i.e. crack, and the red colour (BDSTAT=1) represents fully bonded region. It is evident that the crack initiates at the obtuse corner of the brace initially. The crack front propagates in a triangular pattern towards the end of the brace, eventually aligning perpendicular to the axis of the brace, until sudden failure at the peak load. The crack on the chord initiates around the intersection between the chord and braces, propagating in a elliptical pattern towards the centre of the chord.

Step 2: run models with artificially replicated crack patterns.

The crack growth driving forces, namely the SERRs, need to be obtained at the predetermined crack fronts. Artificially replicated crack patterns for SERR calculation are created on the chord and braces based on the static modelling results as shown in Fig. 12 (a). It should be noted that the crack shape on the chord is assumed to be a semi-circle around the intersection between the chord and brace for simplification, even though it initiates around the sharp corner. While the crack patterns are predetermined, the relationship between L_b and L_c under cyclic loading is still unknown. Crack growth on the brace is solely driven by the SERR values on the brace. However, the SERR distribution on the brace can be influenced by the crack length on the chord, and vice versa. In order to form the basis for predicting the interactive crack growth on the chord and braces, a total of 42 models are run following the model matrix with different combinations of crack lengths on the chord and brace as illustrated in Fig. 12 (b). The relationship between L_b and L_c will be assumed initially and determined based on the SERRs by a iterative procedure in the following algorithm.

Step 3: extract SERR values at the crack fronts and form the SERR surfaces.

SERR values of different fracture modes are extracted at crack fronts for different models. Typical SERR distributions along the crack fronts of 4 extreme combinations of crack lengths on the chord and braces of the joint, L_{c_min}- L_{b_min}, L_{c_min}- L_{b_max}, L_{c_max}- L_{b_min}, L_{c_max}- L_{b_max}, are shown in Fig. 13. In this figure, the SERR distributions are plotted against the normalized distance along the crack fronts (true distance from the edge of the brace divided by the total length of the crack front). It can be found out that the shear fracture mode dominates the crack growth both on the chord and braces. In other words the mode I SERR component is
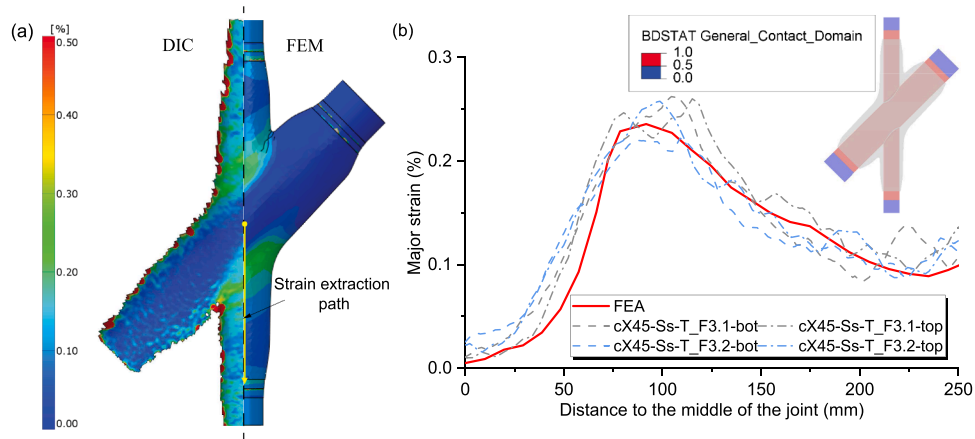
Fig. 7. Comparison of strain distribution on the surface of composite wrap between DIC and FEA (at 165 kN).
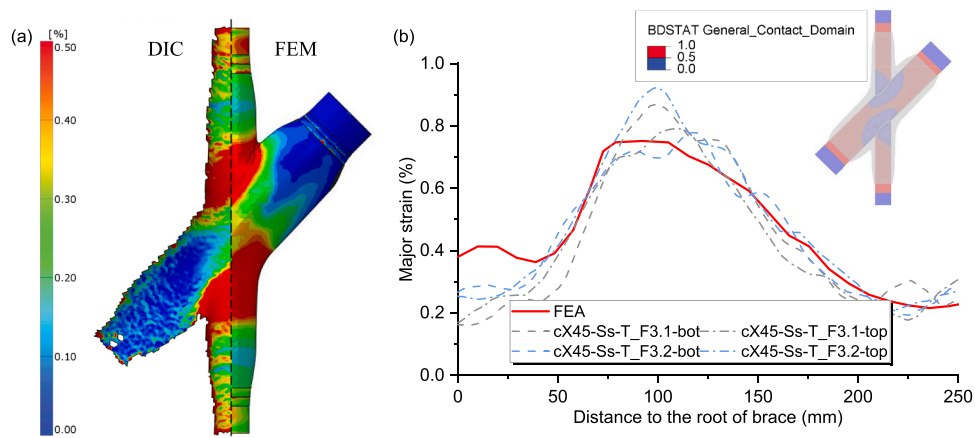

Fig. 8. Comparison of strain distribution on the surface of composite wrap between DIC and FEA (at 300 kN).
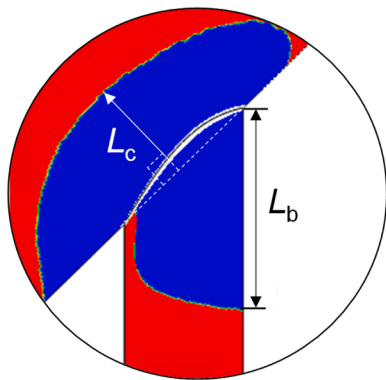

Fig. 9. Definition of crack length on the chord and brace.

Fig. 10. Flowchart of the stationary crack growth method.

limited. Specifically, the mode II fracture behaviour dominates the crack growth on the brace, although a small portion of mode III SERR component is also found when the L_b is small. On the chord, however, equivalent amount of mode II and mode III SERR components arise at the crack tips regardless the crack length. It should be noted that the mode III SERR, which is due to out-of-plane shear behaviour at the interface, may arise due to simplified semi-circle crack shapes on the chord. It is also proved in literature that the crack growth rates can be more than 2 orders of magnitude lower under mode III fracture dominated case [37,38] compared to the mode II dominated case. Considering the insignificant contribution of mode III SERR and for

simplification reason, only the mode II SERR components are considered during the following analysis.

Normally crack growth at a specific location should be driven by the SERR values at the corresponding point [39]. However, the simplified crack shapes may cause unrealistic SERR values at the point where the crack length is defined. An effective SERR value is defined as follows,
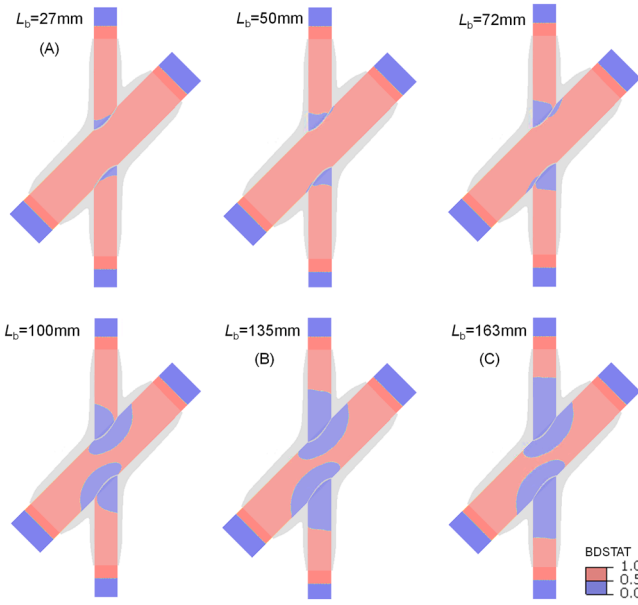
Fig. 11. Debonding crack pattern at different loading stages in the elastic model.

shown in Fig. 13. Such an integral approach is used to consider the fact that each point at the crack tip cannot grow independently and will be influenced by the adjacent portions. In this definition, the SERRs are averaged in a region where the value is above the crack growth threshold (the pink region in Fig. 13). Another option is to simply average the SERR along the entire crack tip. A sensitivity analysis on the influence of SERR definition method will be conducted in Section 4.3.

The effective SERR variation on the brace and chord under different crack length combinations at the load level of 165 kN is shown in Fig. 14. In this figure, the SERR surface is formed by interpolation among the discrete points (red points) obtained from each model. The spline interpolation method is used here and the sensitivity analysis on the interpolation method will be discussed in Section 4.3. Fig. 14 (a) shows that the effective SERR on the brace is mainly influenced by L_b, whereas the influence from L_c is significant only in the case where L_b is small. Fig. 14 (b) shows that the effective SERR on the chord is mainly influenced by L_c while influence from L_b is minimal. The variation of SERR is caused by several factors such as the thickness of the composite wrap, friction at the interface, effective length on the crack tip for averaging the SERR values, etc. For instance, a larger crack length corresponds to the location where the composite wrap is thinner and more significant friction effect. A thinner composite can lead to increased SERR values whereas more friction effect may lead to reduced SERR values. It should be noted that some crack length combinations doesn't

exist actually but a certain crack growth relationship between L_b and L_c needs to be determined in the following steps.

Step 4: selection of FCG curves and prediction of crack growth.

The crack growth on the chord and braces is realized in the algorithm through an iterative procedure as illustrated in Fig. 10. Before that the FCG curve needs to be determined based on the characterized properties in Section 2.1 and interpolated according to the roughness measurement results on the surface of the steel tubes. One typical FCG curve interpolation result is illustrated in Fig. 15, where Fig. 15 (a) shows the basic power law curves and Fig. 15 (b) shows the total life FCG curves interpolated for small scale joints with high roughness level. For the basic power law curves, the exponent C parameter is obtained by substituting the measured roughness parameter S_q into the equation in Fig. 1(d). For the total life FCG curves, the fracture toughness G_c is obtained by substituting S_q into the equation in Fig. 1(b). The SERR threshold G_{th} is assumed to be a portion of G_c. The portion of G_{th} and the curvature exponent D_1 and D_2 parameters is calibrated by the test results of small scale joint. A sensitivity analysis on these two parameters, G_{th} and D_1/D_2, is conducted in Section 4.3.

An initial relationship between L_b and L_c is assumed in the beginning of the iterative procedure as shown in Fig. 16 (a). The number of cycles needed for crack growth on the brace and chord is calculated respectively by numerically integrating the FCG equation (either Eq. (1) or Eq. (2)), based on the SERR values corresponding to each point on the assumed relationship. The numerical integration of the basic power law and total life FCG equation is realized based on the equations below:

$$N_i = \sum_0^i \Delta N_i = \sum_0^i \frac{\Delta a}{C\left(\Delta G_{II,i}\right)^m} \tag{4}$$

$$N_i = \sum_0^i \Delta N_i = \sum_0^i \frac{\Delta a\left[1 - \left(\frac{\Delta G_{II,i}}{G_c}\right)^{D_1}\right]}{C\left(\Delta G_{II,i}\right)^m\left[1 - \left(\frac{G_{th}}{\Delta G_{II,i}}\right)^{D_2}\right]} \tag{5}$$

where N_i represents the number of cycles needed for crack growth on the chord or brace to the ith discrete point in the L_b vs. L_c curve. It is obtained by summing ΔN_i, the number of cycles needed for crack growth within a unit crack length Δa (1 mm in this case), from 0 mm to the current crack length. $\Delta G_{II,i}$ represents the SERR values on the chord or brace at the corresponding crack length. A new relationship between L_b and L_c is obtained based on the cycles calculation. The whole procedure is iterated until the relationship between L_b and L_c is stabilized.

The example of stabilized relationship between L_b and L_c is plotted together with the SERR surfaces of the brace and chord in Fig. 16 (b). This figure can clearly show the competing of crack growth on the brace and chord driven by the SERR values. In the beginning, where L_b and L_c are near 0 mm, G_{II} on the brace is higher, thus leading to dominated crack growth on the brace. The crack growth on the chord becomes
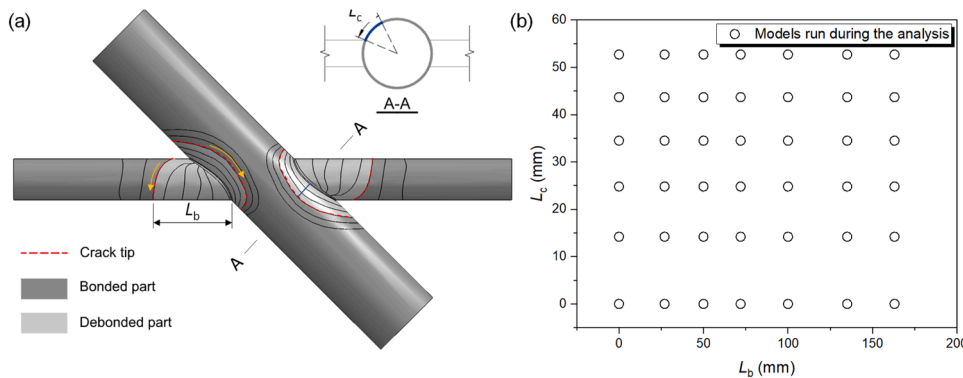

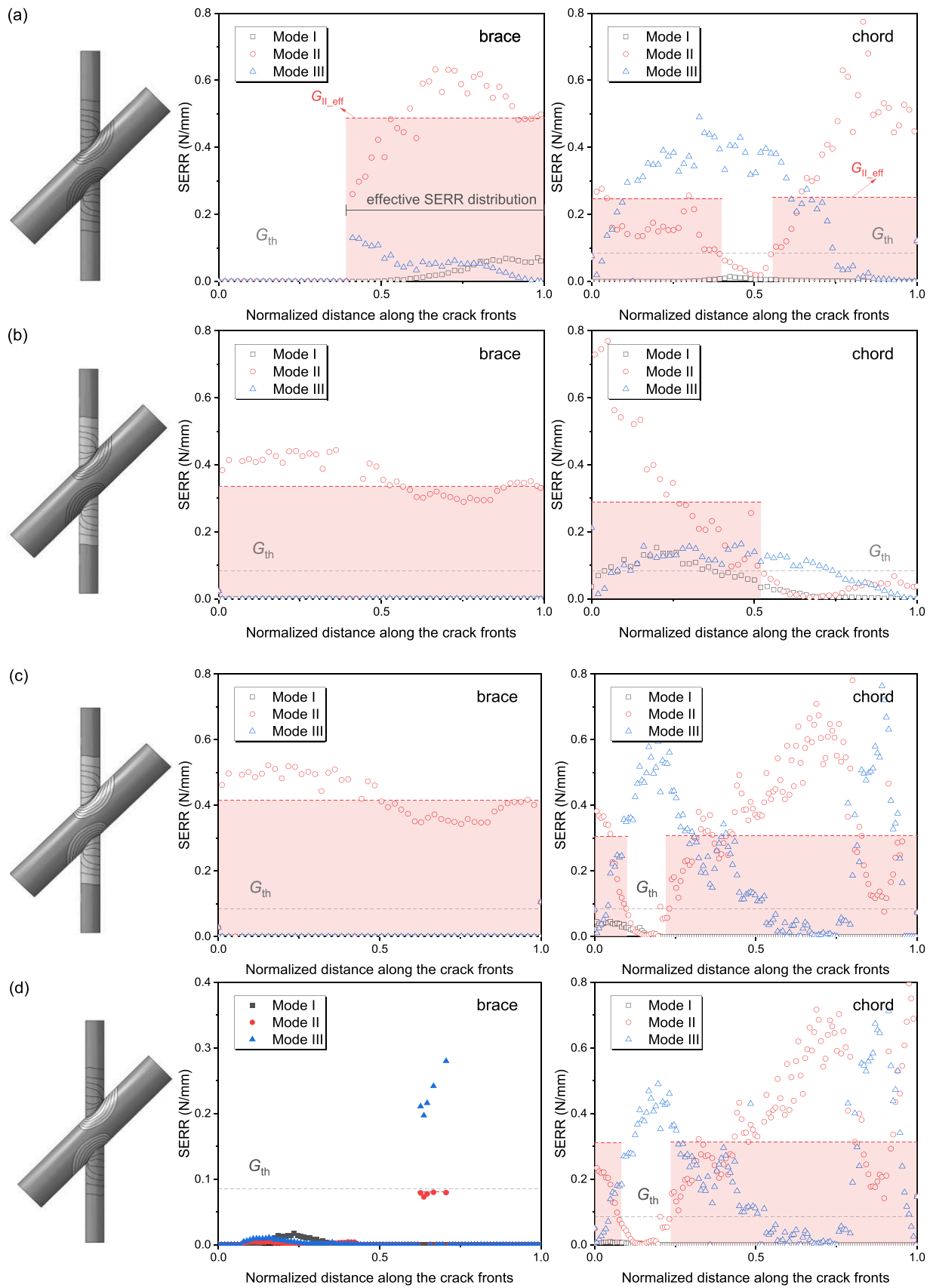**Fig. 12.** Artificially replicated crack pattern in the FE model.

Fig. 13. SERR components and distribution along crack fronts on the chord and braces (a) $L_{\text{c\_min}}$- $L_{\text{b\_min}}$; (b) $L_{\text{c\_min}}$- $L_{\text{b\_max}}$; (c) $L_{\text{c\_max}}$- $L_{\text{b\_min}}$; (d) $L_{\text{c\_max}}$- $L_{\text{b\_max}}$.
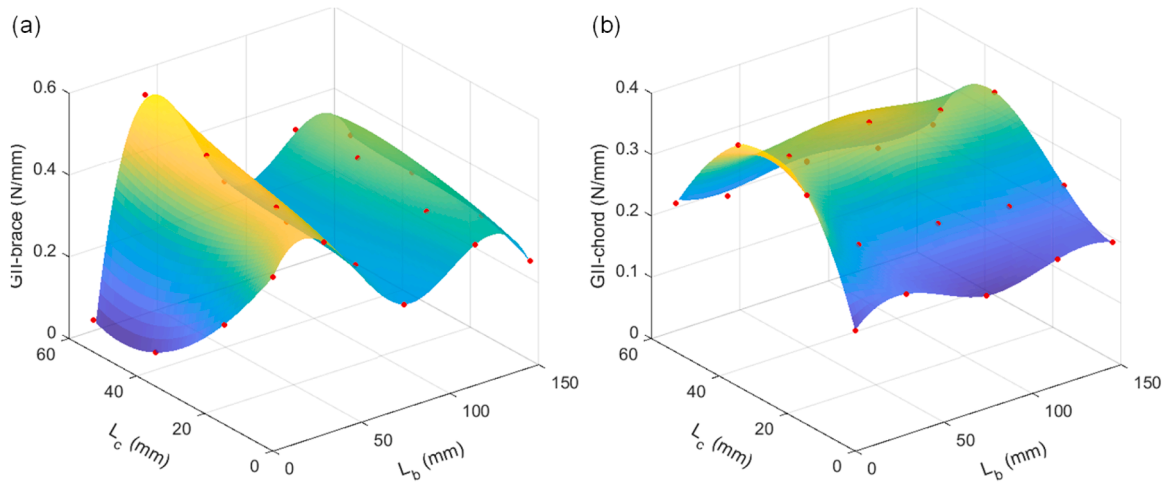
Fig. 14. Mode II SERR surface of the chord and brace at 165 kN (a) G_{II} on the brace; (b) G_{II} on the chord.
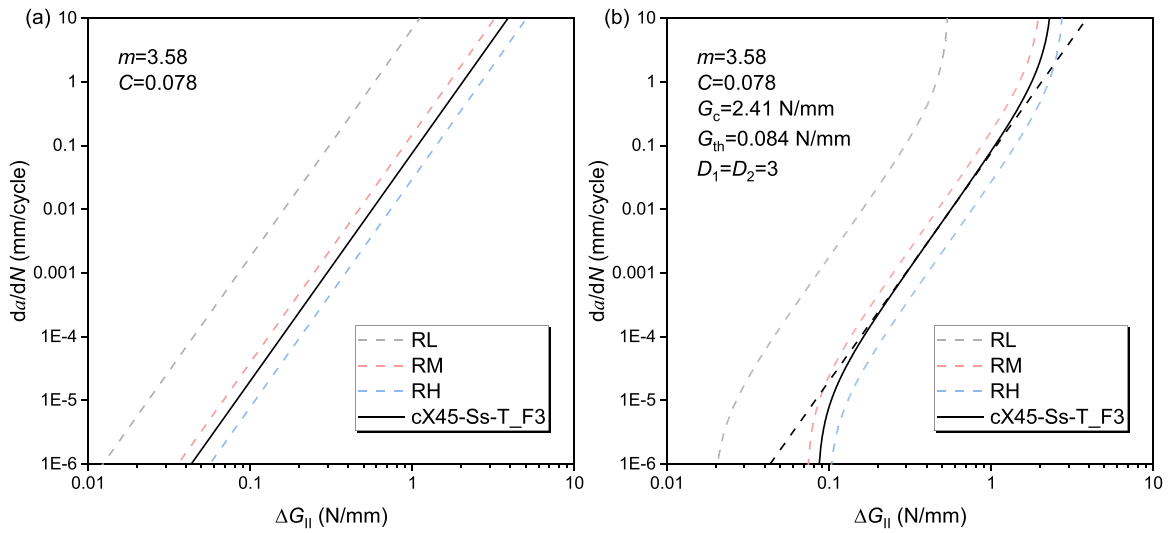

Fig. 15. Interpolation of FCG curves between different roughness series (a) Paris curves; (b) total life FCG curves.
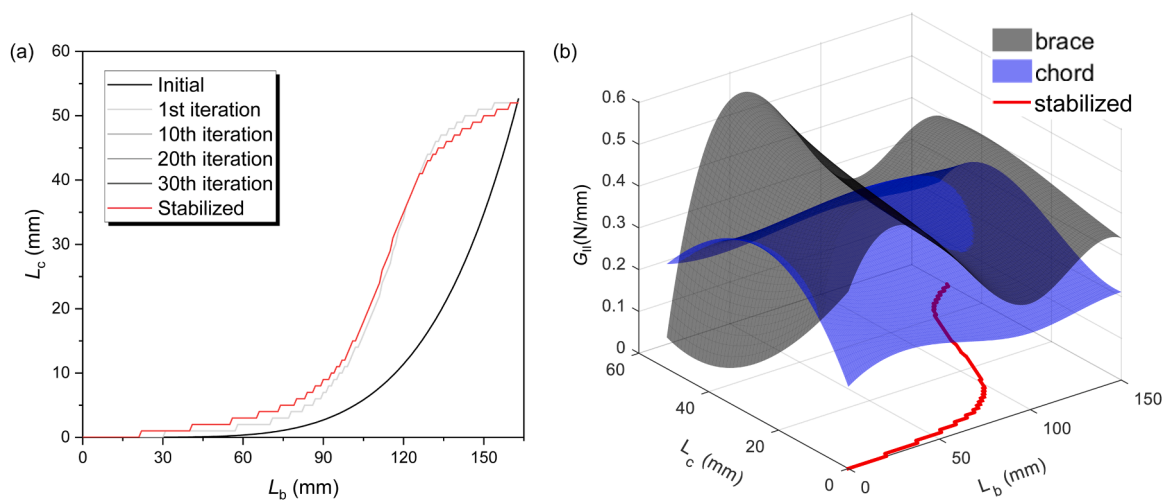
Fig. 16. Iteration of relationship between L_b and L_c (a) iteration procedure; (b) the stabilized relationship plotted with SERR surface.

dominated as the G_{II} on the chord becomes higher than that on the brace at around $L_b \approx 110$ mm and $L_c \approx 30$ mm. After that crack growth on the brace becomes faster again due to variation of the SERR. Based on the obtained relationship between L_b and L_c, the stiffness degradation of the joint can be obtained by extracting the initial stiffness of corresponding models afterwards.
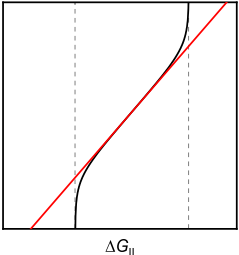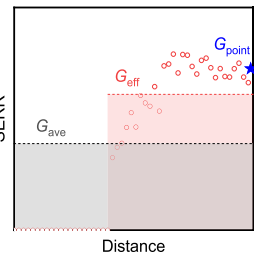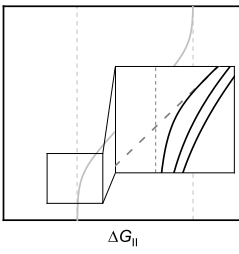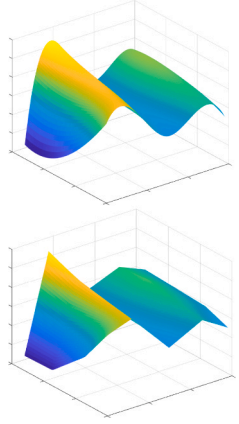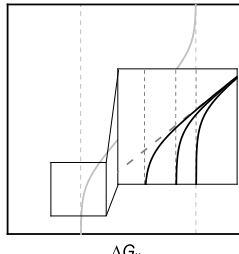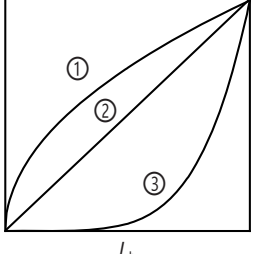
4. Model calibration

In this section, the FE model is calibrated based on the small scale joint tests listed in Table 1. Modelling results with the optimized (calibrated) parameters (the FCG model, curvature exponent D, threshold SERR G_{IIth}, SERR equivalent method, SERR interpolation method, and the initial relationship between L_b and L_c) underlined in Table 4 are shown in Sections 4.1 and 4.2. Sensitivity studies for each parameter will be discussed in Section 4.3.

4.1. Crack growth

Based on the average measured roughness in Table 1, the interpolated FCG curves for different roughness series are shown in Fig. 17. SERR surfaces on the brace and chord for each series are shown in Fig. 18. The SERR surfaces for series (b) and (c) are the same and shown in Fig. 18 (b) since the roughness level does not influence the SERR value. The stabilized relationships between L_b and L_c are also shown in the same figure as the red curve. It can be seen that under relatively low load level, crack at the interface mainly grows on the brace, whereas crack on the chord remains undeveloped. On the contrary, cracks on the chord and brace grows simultaneously under relatively higher load levels. It should be noted that SERR values in case (b) do not increase proportionally as the load increases compared to case (a), although all materials are in the linear elastic stage. This is due to the difference in the crack growth pattern (relationship between L_b and L_c) and contractions of composite wrap under different load levels.

Table 4
Parameter matrix for sensitivity analysis.

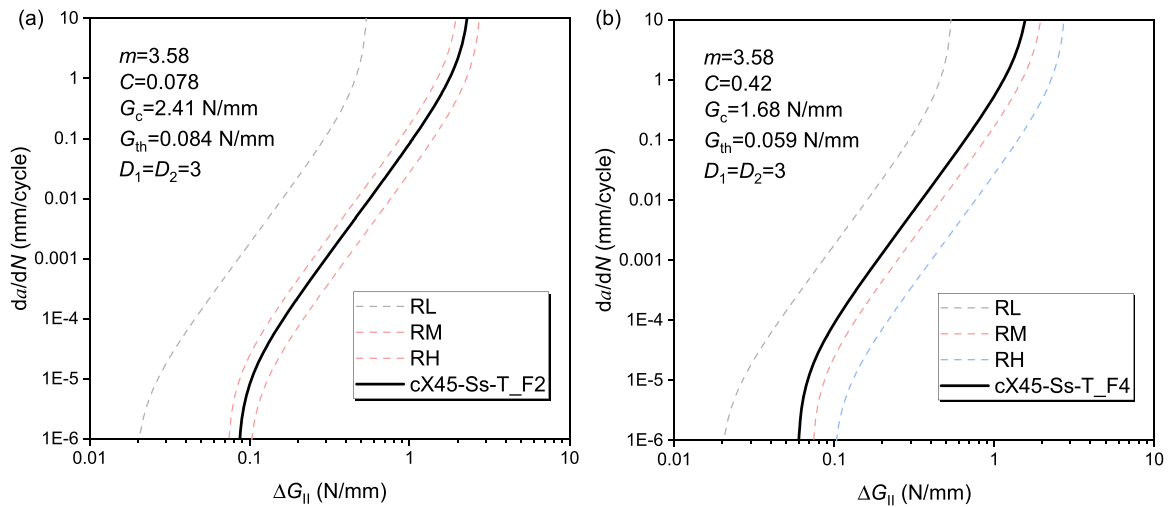| Input FCG parameters			Modelling techniques		
Parameter	Sketch	Value	Parameter	Sketch	Value
FCG model		Power law, Total life FCG	Equivalent SERR		G_{ave}, $\underline{G_{eff}}$, G_{point}
Curvature exponent, D		$\underline{3}$, 5, 7	SERR interpolation method		Spline, Linear
Threshold SERR, G_{th}		1 % G_c, $\underline{3\ \%\ G_c}$, 5 % G_c	Initial relationship between L_b and L_c		Convex, Linear, Concave

Fig. 17. Obtaining total life FCG model parameters for different roughness series (a) high roughness, $S_q = 16.78$ µm; (b) low roughness, $S_q = 10.98$ µm.
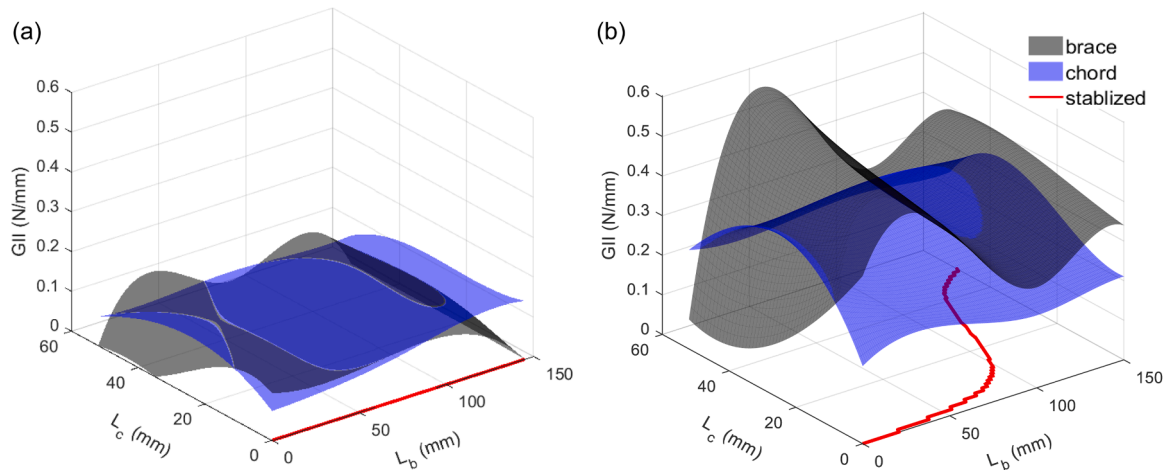

Fig. 18. SERR surface and stabilized relationship between L_b and L_c (a) small scale joints with high roughness under 10–110kN; (b) small scale joints with high/low roughness under 15–165kN;.

Crack growths on the braces of each series of specimens modelled by the FE model are plotted against the test results in Fig. 19, which is obtained based on the combined DIC-FEA method introduced in **Ref.** [6]. The figure shows that the modelling results overlap well with the test results for most of the cases, especially at the early loading stages. However, cracks grew with different rates on the top and bottom braces during the tests as shown in **Ref.** [6] and also in Fig. 19 (b), where the FEA results deviate significantly from the test results after 35,000 cycles. This might be result from different interface conditions, such as roughness, initial defects etc. in different braces, which cannot be considered in the FE model.

4.2. Stiffness degradation

In the model matrix shown in Fig. 12, the elastic stiffness of each model is extracted, forming the 'stiffness surface' similar to the SERR surface. The stiffness degradation of the joints as the crack grows thus can be obtained by interpolating the stiffness value within the stiffness surface and compared with the test results in Fig. 20. The comparison shows that the FEA results generally match well with the test results.

More detailed comparison between FEA results against test results in terms of fatigue lives are conducted by taking every 1 % stiffness degradation (from 1 % to 40 % for high load level, from 1 % to 10 % for

low load level) as failure criterions shown in Fig. 21. The figure shows that the relative error of the two in the logarithmic space is within 20 % for all the cases. The coefficient of determination expressed in Eq. (6) are higher than 0.6 except for the case of small scale joints with low roughness level, case (c).

$$R^2 = 1 - \frac{\sum_i (y_i - f_i)^2}{\sum_i (y_i - \overline{y})^2} \tag{6}$$

where y_i is the test results, $\overline{y}$ is the average value of the test results and f_i is the modelling results.

The negative R^2 value for case (c) results from the different stiffness degradation trends between the test and FEA results as shown in Fig. 20 (c). The simulated fatigue life underestimates the test results, i.e. the predicted stiffness degrades faster, under the failure criterion of 10 % and overestimates the test results under failure criterion of 20 % and 40 %, respectively. It should be noted that the variation of the stiffness degradation can be influenced by the surface conditions of the steel tubes, thickness of the composite wrap and possibly the temperature variation during the fatigue test, etc. Meanwhile, the stiffness degradation trend obtained by FEA is driven by the SERR variation shown in Fig. 18, which cannot take those influential factors into account.
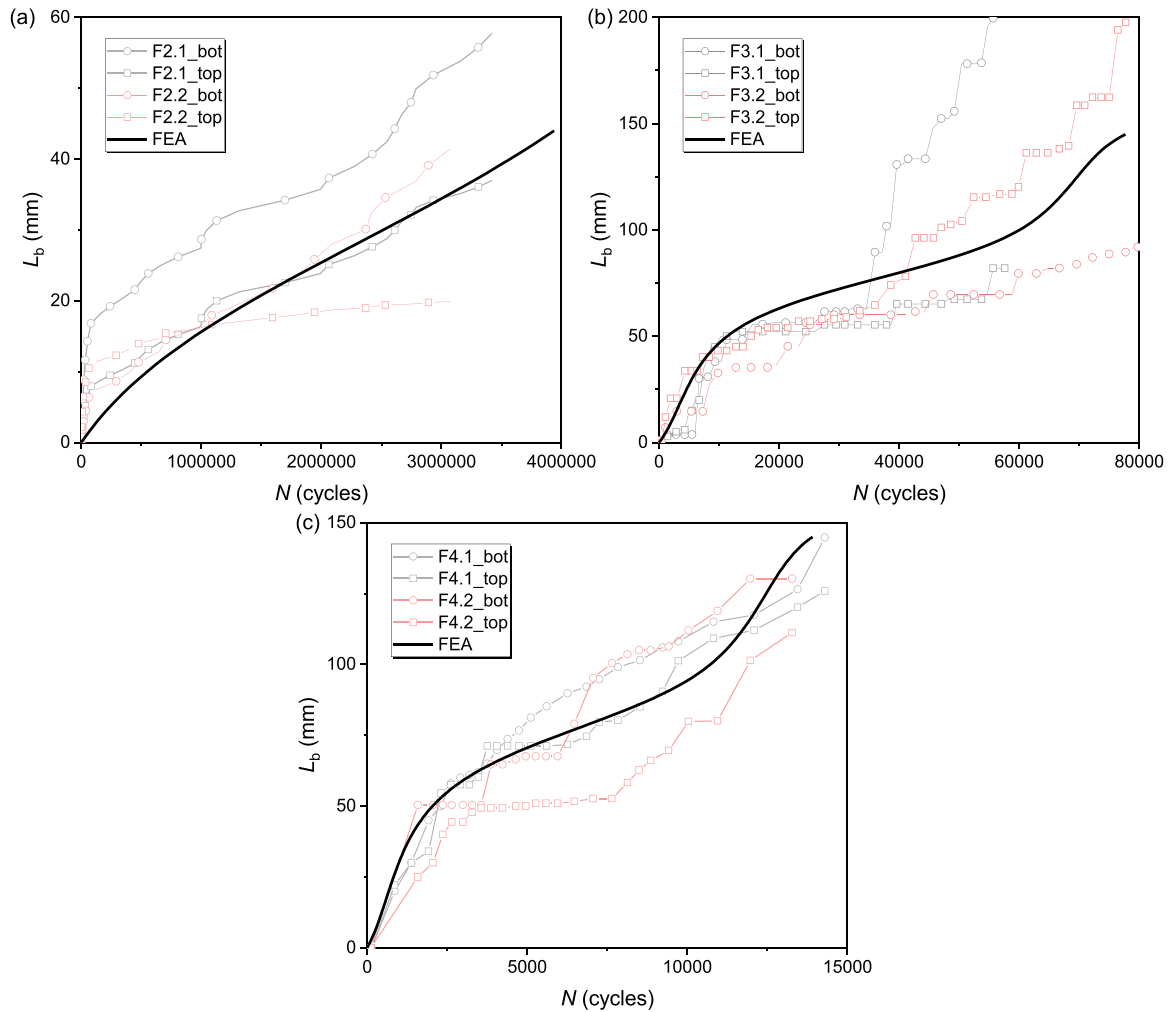
Fig. 19. Comparison of crack growth on the brace between test results and FEA (a) small scale joints with high roughness under 10–110kN; (b) small scale joints with high roughness under 15–165kN; (c) small scale joints with low roughness under 15–165kN.

4.3. Sensitivity analysis on modelling parameters

While FEA results match well with the test results based on the optimized combination of parameters, each parameter can have significant or insignificant influence of the modelling results. Sensitivity analysis on each key modelling parameter is conducted in this section to investigate its influence and rationalize the choice of the optimized value.

Investigated parameters are divided into two categories, namely the input FCG parameters and the modelling techniques, with the definitions and ranges of each parameter shown Table 4.

4.3.1. Influence of FCG model

As discussed in Section 2.1, the fatigue crack growth properties can be expressed in two different ways, the basic power law function Eq. (1) and the total life model Eq. (2). The influence of adopting different FCG models on the simulated results are compared in this section. Fig. 22 shows the interpolated power law and total life model for joint with the high roughness level. The SERR ranges experienced by the joint under two different load levels, extracted from the SERR surface, are also shown in this figure. It shows that the SERR range is between 0.2–0.5 N/mm under 15–165kN, where two FCG models overlap with each other. Whereas the SERR range is close to G_{th} under 10–110kN, between 0.075–0.15 N/mm, where the power law is above the total life FCG model.

Fig. 23 shows the modelling and test results of the joint under 15–165kN. The difference of modelling results, namely the crack growth and stiffness degradation, based on the power law and total life FCG model, is insignificant. Both results match well with the test results due to the fact that two FCG models overlap in this SERR range. However, modelling results based on these two models are significantly different under 10–110kN as shown in Fig. 24. The crack growth and stiffness degradation is overestimated thus shorter fatigue life is obtained by using the power law, while modelling results based on the total life FCG model match well with the test results. This is due to the fact that the power law is above the total life FCG model around the relatively low SERR range thus the crack growth rates are overestimated.

Considering the fact that using power law may overestimate the crack growth when the SERR level is near the threshold, the total life FCG model is adopted in the following analysis.

4.3.2. Influence of curvature exponent D and SERR threshold

It has been shown from the previous section that the total life FCG model can well reproduce the test results in terms of crack growth and stiffness degradation for the case where SERR range is near the threshold G_{th}. However, the matching quality still depends on the curvature of the FCG curve in the subcritical region, which is determined by the curvature exponent D and threshold ratio G_{th}/G_c. As shown in Fig. 25 (a), the total life FCG model becomes closer to the power function, leading to higher crack growth rates, in the threshold region as D increases.
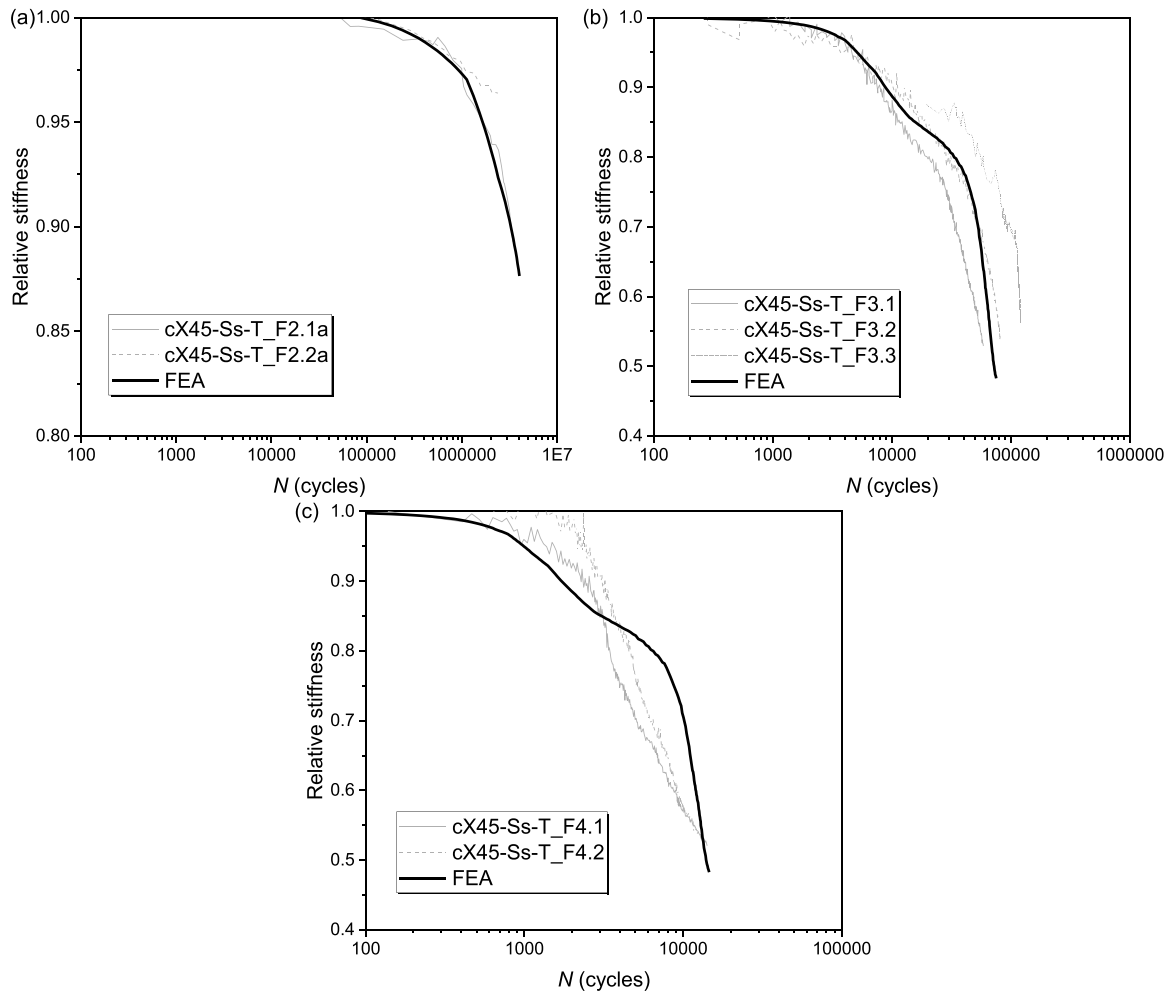
Fig. 20. Comparison of stiffness degradation between test results and FEA (a) small scale joints with high roughness under10–110kN; (b) small scale joints with high roughness under 15–165kN; (c) small scale joints with low roughness under 15–165kN.
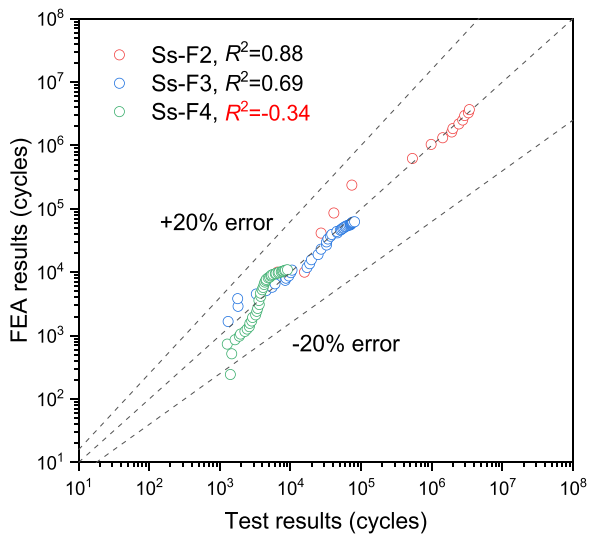

Fig. 21. Comparison of fatigue lives under different failure criterion between test and FEA results.
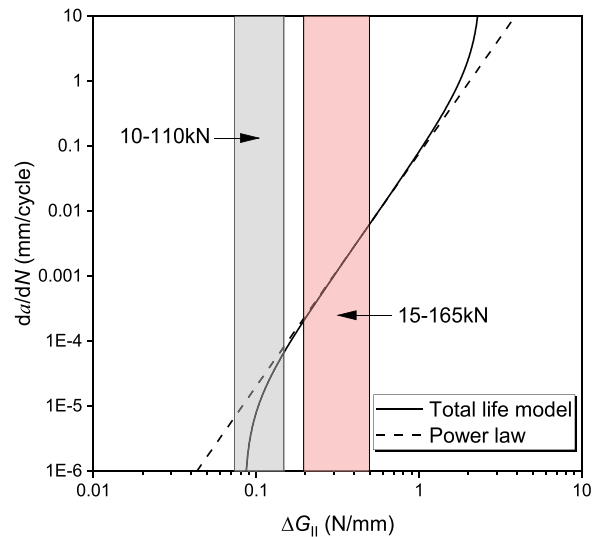

Fig. 22. Comparison of SERR range under 10–110kN and 15–165kN for small scale joints.

Meanwhile, as shown in Fig. 25 (b), the total life FCG model becomes further away from the power function, leading to lower crack growth rates, in the threshold region as G_{th} increases. A sensitivity study is

conducted in this section to find the optimal combination of these two parameters, which can help reproduce test results for all three cases.

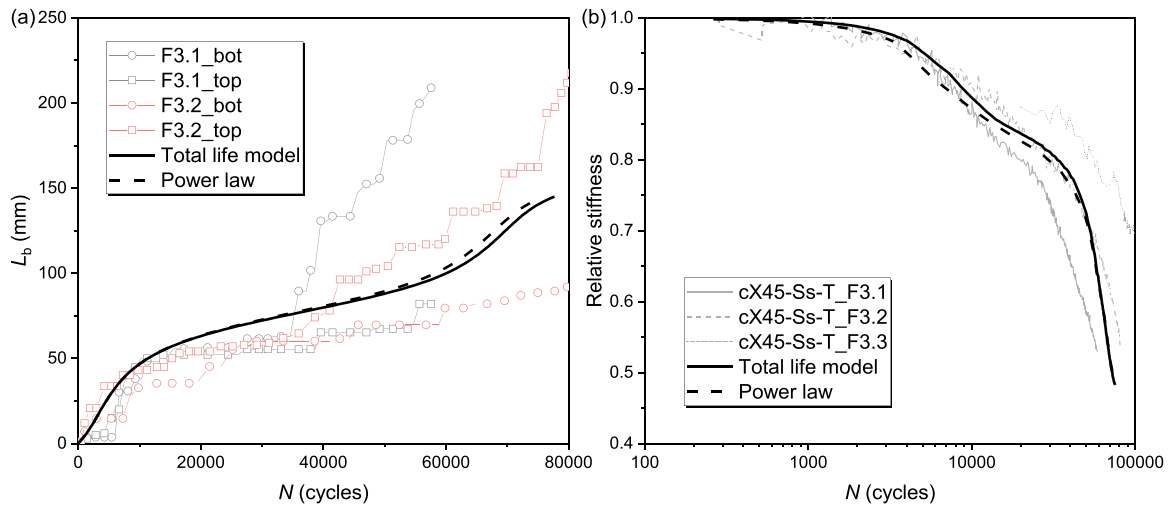It has been confirmed from Section 2.1 that the curvature exponent D

Fig. 23. Comparison between modelling results by total life model and Paris curves on small scale joints under 15–165kN (a) crack growth; (b) stiffness degradation.
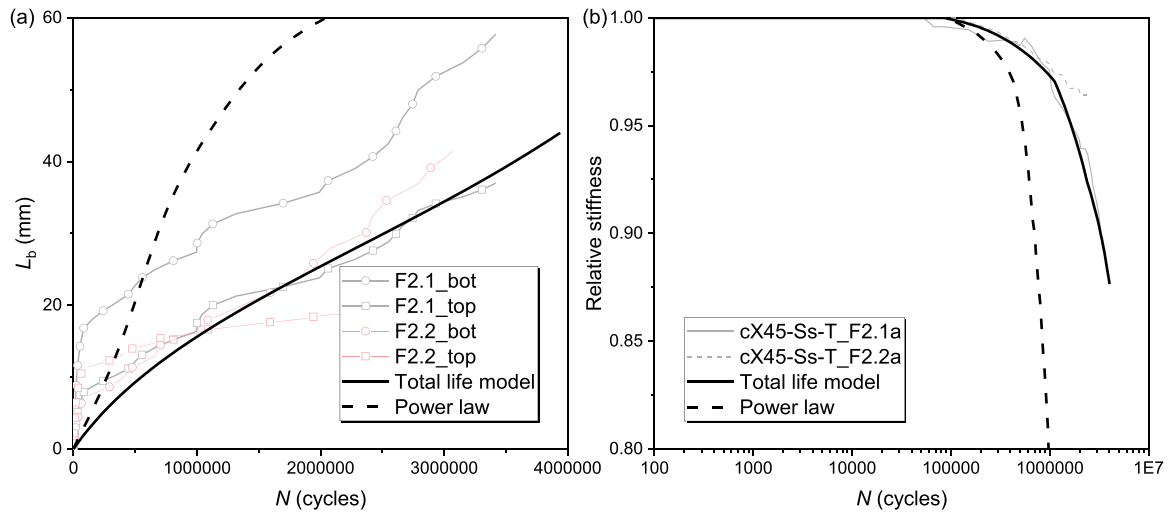

Fig. 24. Comparison between modelling results by total life model and Paris curves on small scale joints under 10–110kN (a) crack growth; (b) stiffness degradation.
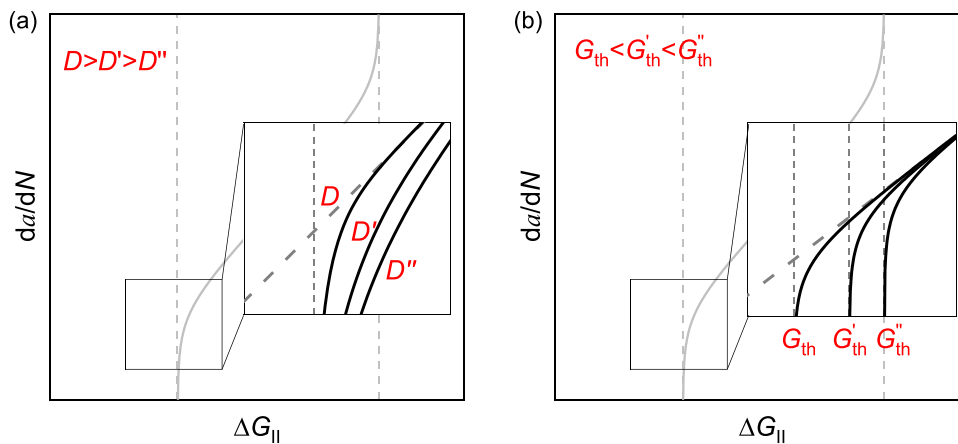

Fig. 25. Influence of (a) curvature exponent D and (b) threshold G_{th} on the shape of total life FCG model.

above 3 can lead to the same fitting quality for the 4ENF test data as that based on the power function. Meanwhile, the threshold ratio can be 1 %–9 %. D values of 3, 5, 7 in combination with the threshold ratios of

1 %, 3 %, 5 % are adopted to investigate their influence on the modelling results of stiffness degradation of the joint. The optimal combination of these two parameters should lead to relatively good matching

quality for all the 3 test cases. The matching quality of the modelling results with the test data is evaluated by the coefficient of determination, R^2, which is obtained by comparing the fatigue lives using different failure criterions as shown in Eq.(6) and Fig. 21.

The R^2 values for all the 3 test cases using different combinations of D and G_{th}/G_c are shown in Fig. 26 (a). R^2 values below 0 are shown as equal to 0. It can be seen that the matching quality for the Ss-F3 series (small scale joints with high roughness under 15–165kN) is always above 0.7 even 0.9 regardless of the combination of the two parameters. This is due to the fact that the SERR values experienced by the joint during the test are in the range where the total life FCG model overlaps with the power function. The curvature of the total life FCG model near the threshold will not influence the crack growth rate in that region. On the contrary, the matching quality for the Ss-F4 series (small scale joints with low roughness under 15–165kN) is always bad (below 0) due to the different variation trends between the test data and modelling results as discussed above. The only test case that is rather sensitive to the D and G_{th}/G_c values is the Ss-F2 series (small scale joints with high roughness under 10–110kN), who experienced the SERR range between 0.075–0.15 N/mm during the test as shown in Fig. 22. Any deviation of the ratio G_{th}/G_c away from (higher or lower than) 3 % can lead to R^2 below 0. Meanwhile, the matching quality may deteriorate as the D value increases from 3 to 7 at G_{th}/G_c= 3 %.

In order to evaluate the overall matching quality for all the test cases, an equivalent R^2, which is the geometric mean value for 2 test cases (Ss-F4 series is excluded considering the mismatch of stiffness degradation trend) expressed in Eq. (7) is adopted:

$$R_{eq}^2 = \sqrt{R_1^2 R_2^2} \tag{7}$$

where R_1^2, R_2^2 are the coefficients of determination for Ss-F2 and Ss-F3 series, respectively. As shown in Fig. 26 (b), the combination of D= 3 and G_{th}/G_c= 3 % gives the best matching quality for all the test cases, which will be adopted for the remaining analysis.

4.3.3. Influence of equivalent SERR defining method

As the driving mechanism for crack growth at the interface, it is crucial to choose appropriate SERR values at the crack tip. Whereas the SERR distribution along the crack tip is influenced by the crack shapes. Some unrealistic values may arise at certain locations of the crack tip. Different equivalent SERR defining methods are proposed and compared in this section. The three equivalent SERR defining methods are shown
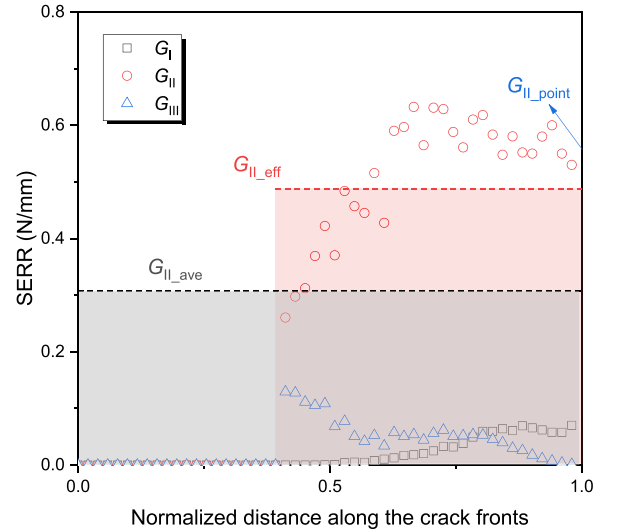

Fig. 27. Different defining methods for SERR on the brace.

in Fig. 27, including 1) point SERR, G_{II_point}, which is the SERR value at the location where the crack length is defined; 2) effective SERR, G_{II_eff}, which is the average value of SERR over the region where SERR values are above G_{th}; 3) average SERR, G_{II_ave}, which is the average value of SERR over the entire length of crack tip. For SERR distributions above G_{th} along the entire crack tip, e.g. when L_b is large enough, G_{II_eff} equals to G_{II_ave}.

SERR surfaces obtained according to the three different methods for small scale joints under 15–165kN are shown in Fig. 28. It can be seen from Fig. 28 (b) that G_{II_ave} on the brace is smaller than G_{II_eff} when L_b is small, where the SERR values are only distributed at a limited region along the crack tip. On the contrary, the point SERR G_{II_point} is usually above the other two average values, thus leading to generally highest SERR surfaces both on the chord and brace as shown in Fig. 28 (c).

Crack growth on the brace and stiffness degradation modelling based on three different equivalent SERR defining methods are compared with test results in Fig. 29. When adopting G_{II_ave}, crack predominantly grows on the chord due to very low SERR values when crack initiates on the brace as illustrated in Fig. 28 (b). This leads to too much longer crack initiation life (with limited stiffness degradation at the initial stage as shown in Fig. 29 (b)), and abrupt stiffness drop at later stage. When
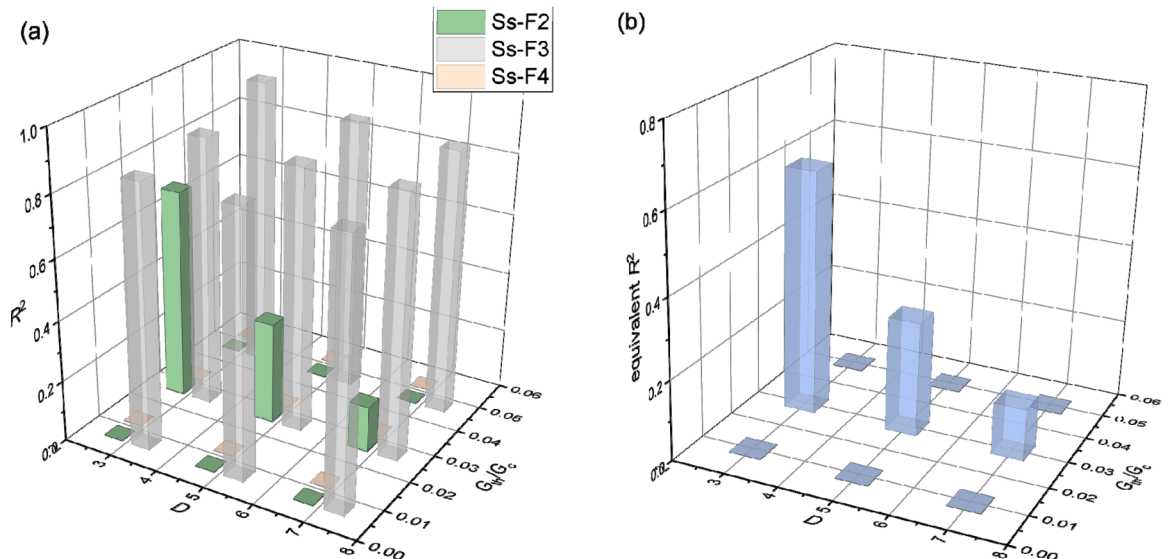

Fig. 26. Coefficient of determination (R^2) versus threshold ratio and curvature exponent D (a) R^2 of each case; (b) equivalent R^2 of all cases.
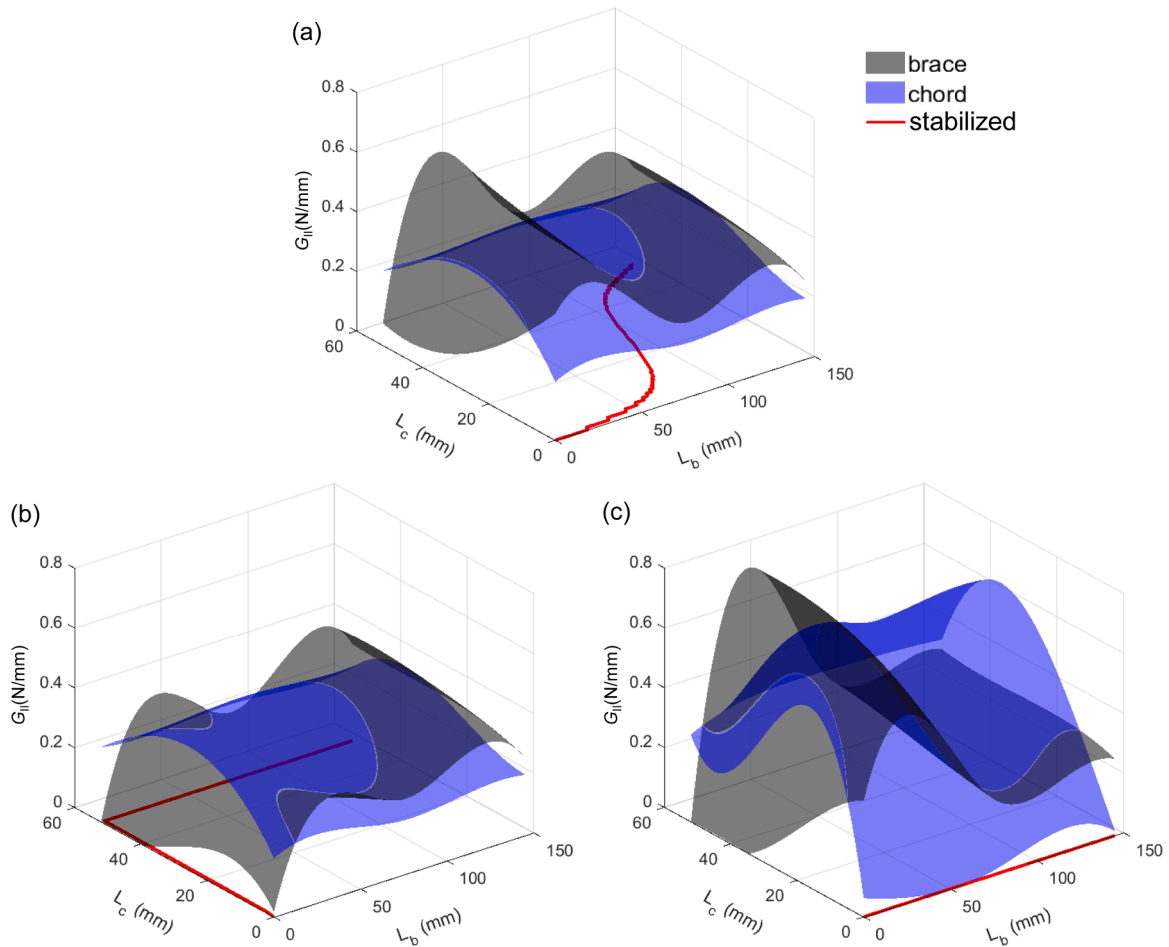
Fig. 28. SERR surface and stabilized relationship between L_b and L_c based on (a) effective SERR G_{II_eff}; (b) average SERR G_{II_ave}; (c) point SERR G_{II_point}.
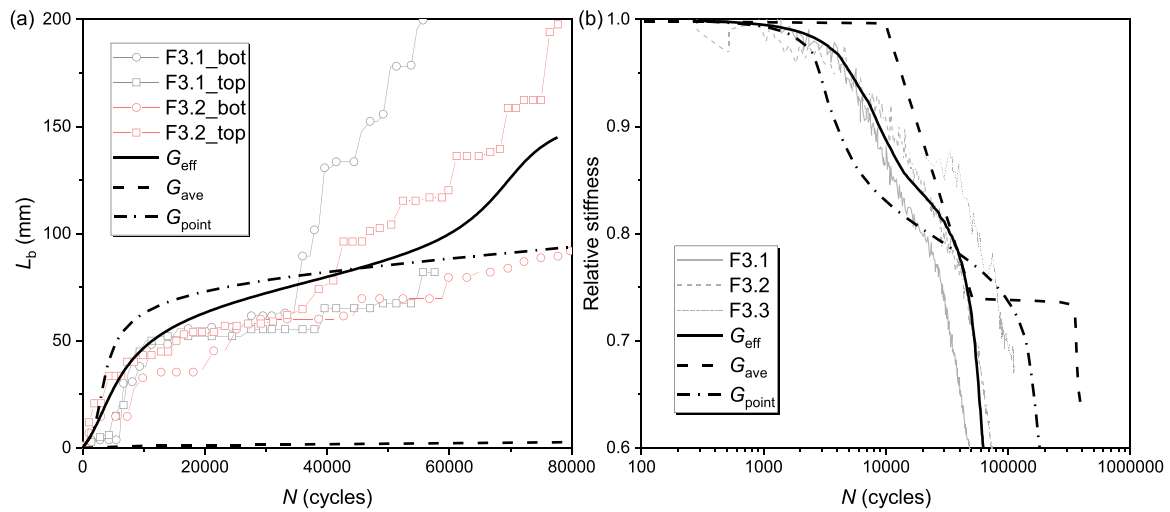

Fig. 29. Comparison of different SERR equivalent methods on (a) crack growth; (b) stiffness degradation.

adopting G_{II_point}, on the contrary, crack predominately grows on the brace due to very low SERR values when crack initiates on the chord as illustrated in Fig. 28 (c). The higher point SERR values on the brace lead to more rapid crack growth thus early stiffness drop as shown in Fig. 29 (b).

In general, the effective SERR can well reproduce the crack growth on the brace and stiffness degradation as test results. It not only works

well for the case of joints with high roughness under 15–16kN, but also leads to good match with test results for other cases as shown in Sections 4.1 and 4.2. The effective SERR is adopted for the remaining analysis.

4.3.4. Influence of interpolation method for the SERR surface

As introduced in Section 3.3, the SERR surfaces are obtained by interpolating specific SERR values obtained from FE models in the

model matrix (Fig. 12). The interpolating method may play an important role in determining the modelling results. Two commonly used methods, linear interpolation and cubic spline interpolation, are compared in this section.

SERR surfaces obtained based on these two methods are shown in Fig. 30 (a) and (b). While smooth surfaces are obtained based on the spline method, surfaces obtained based on linear interpolation exhibit sharp edges. It shows that the stabilized relationships between L_b and L_c (the red curves) are almost identical. Simulated crack growth and stiffness degradation based on these two interpolation methods are shown in Fig. 30 (c) and (d). It shows that both methods match well with the test results, but the linear interpolation method slightly underestimates crack growth and stiffness degradation in the early stage, and overestimates the crack growth and stiffness degradation at the later
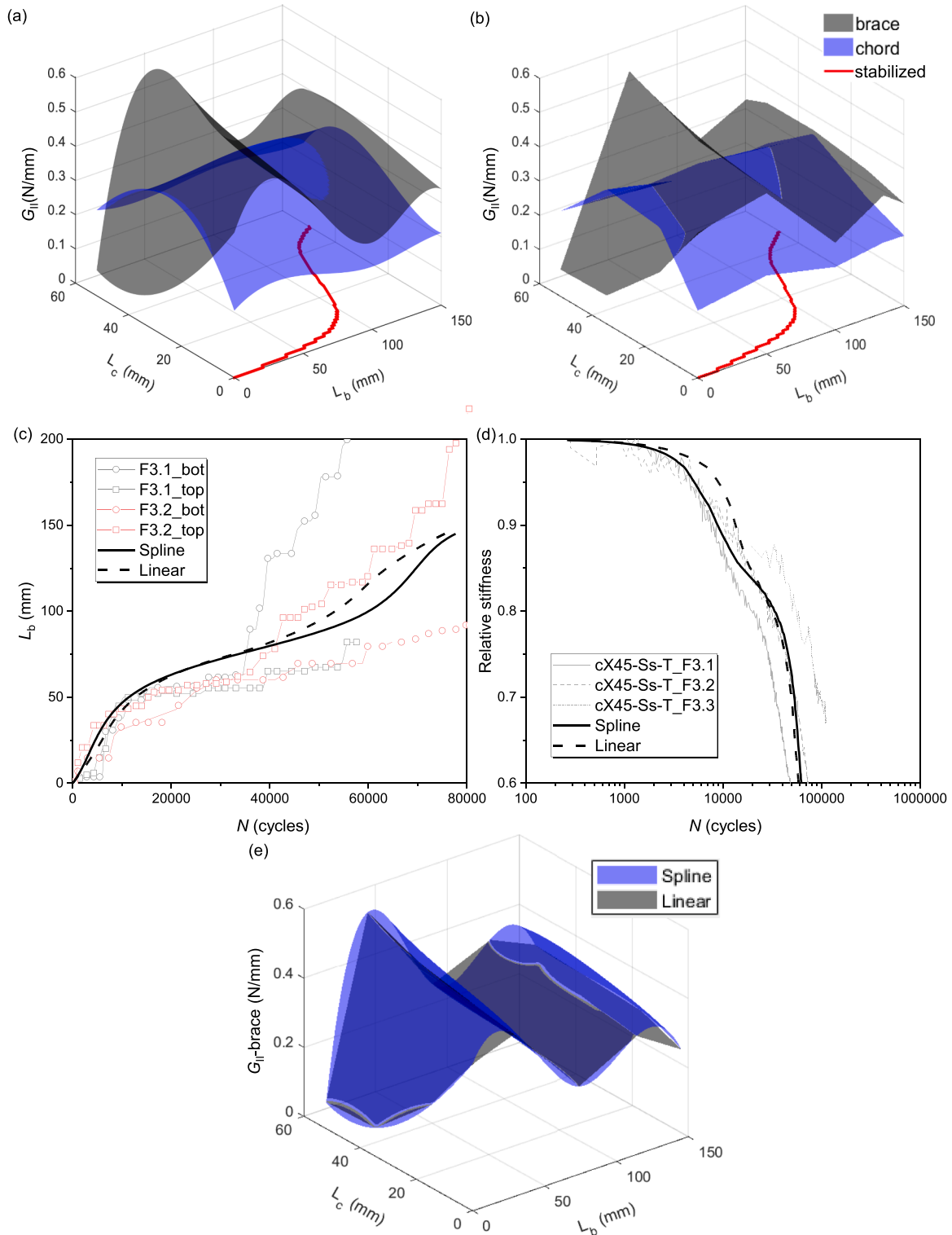

Fig. 30. Comparison of different interpolation methods of SERR surface (a) spline method; (b) linear method; (c) comparison of crack growth; (d) comparison of stiffness degradation; (e) comparison of SERR surfaces.

stages. This may be due to the fact that the linear interpolated surface underestimates the SERR values around the peak of the surface and overestimates the SERR values around the valley of the surface as shown in Fig. 30 (e).

Considering similar results obtained by these two interpolation methods but possible underestimation and overestimation of SERRs based on the linear interpolation method, the spline interpolation method is adopted for the remaining analysis.

4.3.5. Influence of initial relationship between L_b and L_c

Another modelling technique which may influence the results is the initial relationship between L_b and L_c. As shown in Fig. 31 (a), three arbitrary but representative initial relationships, namely linear, convex and concave shapes, are applied for modelling the fatigue debonding behaviour of small scale joints with high roughness under 15–165kN. The results show that the stabilized relationship, crack growth, as well as the stiffness degradation modelled by different initial relationships are identical to each other, indicating that the initial relationship between L_b and L_c will not influence the modelling results. The linear relationship is adopted for the remaining analysis for simplicity.

5. Model validation

In this section, the calibrated FE model is validated against test results of upscaled joints. The upscaled joints experienced debonding at the composite-to-steel interface, resulting in stiffness degradation under cyclic loading. The detailed test results can be found in [40] and will not

be expanded here. The same procedure as described in Section 3.3 is applied to predict the fatigue debonding behaviour. The debonding crack pattern is obtained by loading the elastic model monotonically. The SERR values along the crack tips are extracted afterwards. One typical result of SERR distribution, corresponding to L_b= 157 mm and L_c= 36 mm, is shown in Fig. 32. It can be found out that the crack on the brace is mainly driven by the mode II components, which is generally evenly distributed along the crack tip. SERR distribution on the chord is highly uneven, with a certain portion of mode III components present at the crack tip. However, the effective mode II SERR is used for the analysis, as it has been used for the small-scale joints.

The step-by-step modelling results are presented in Fig. 33. The interpolated FCG curve is shown in Fig. 33 (a). According to Fig. 33 (b), SERR values are higher on the brace when it initiates, but becomes higher on the chord after the crack on the brace stabilizes at around 200 mm. This leads to predominant crack growth on the brace at initial stages but predominant crack growth on the chord at later stages, as shown by the stabilized relationship between L_b and L_c in this figure. The predicted crack growth on the brace is shown in Fig. 33 (c). Due to limited strain development on the composite wrap, it was unfortunately impossible to obtain the crack growth through DIC monitoring system. No monitored crack lengths are present in the figure. Stiffness degradations of the joints were monitored by the LVDT system during the tests and are compared with the modelling results in Fig. 33 (d). It shows that the modelling results generally match well with the test results. A more detained quantitative comparison between the tested and simulated fatigue lives by taking different failure criterions is shown in Fig. 34. It
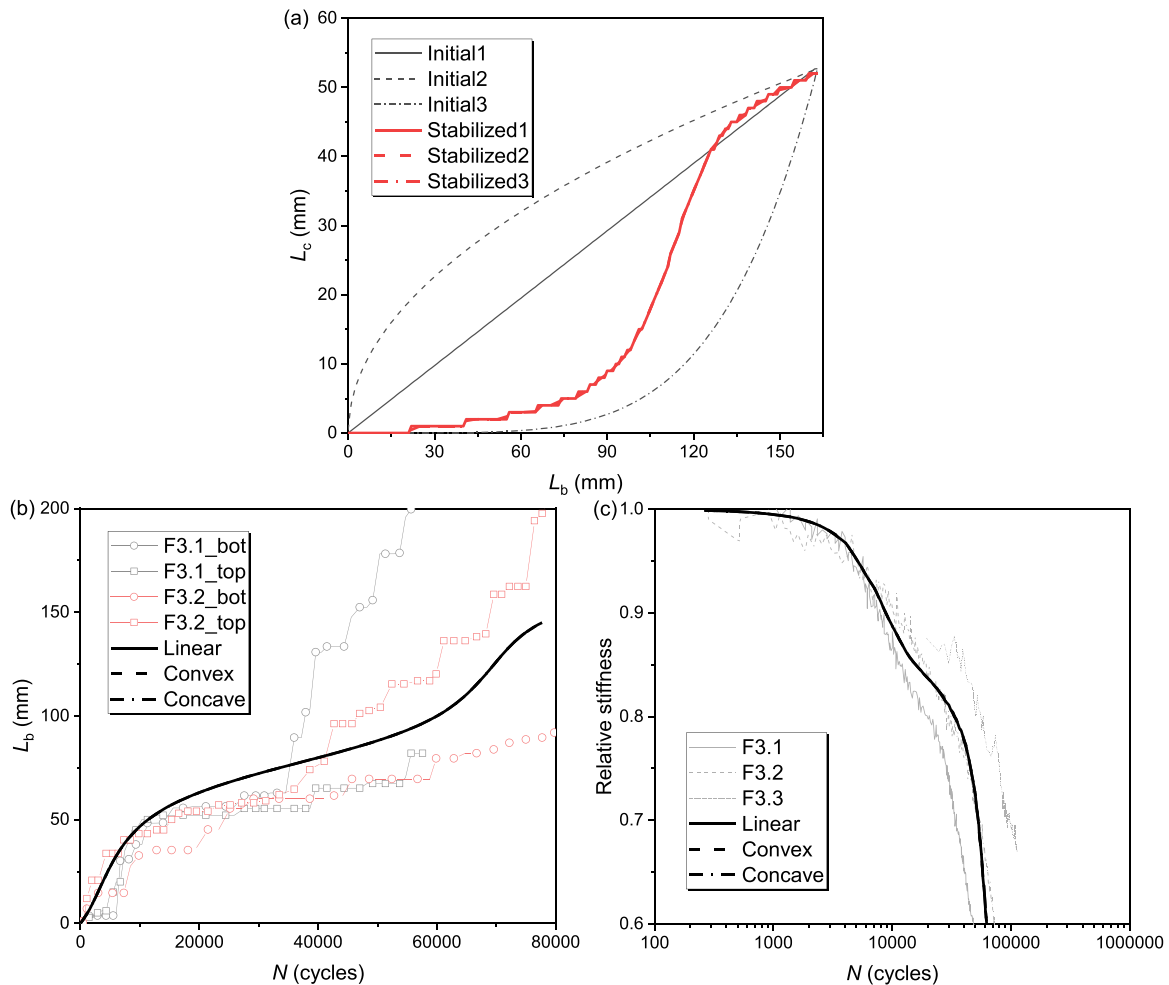

Fig. 31. Sensitivity study on the initial relationship between L_b and L_c (a) initial and stabilized relationship; (b) crack growth based on different initial relationships; (c) stiffness degradation based on different initial relationships.
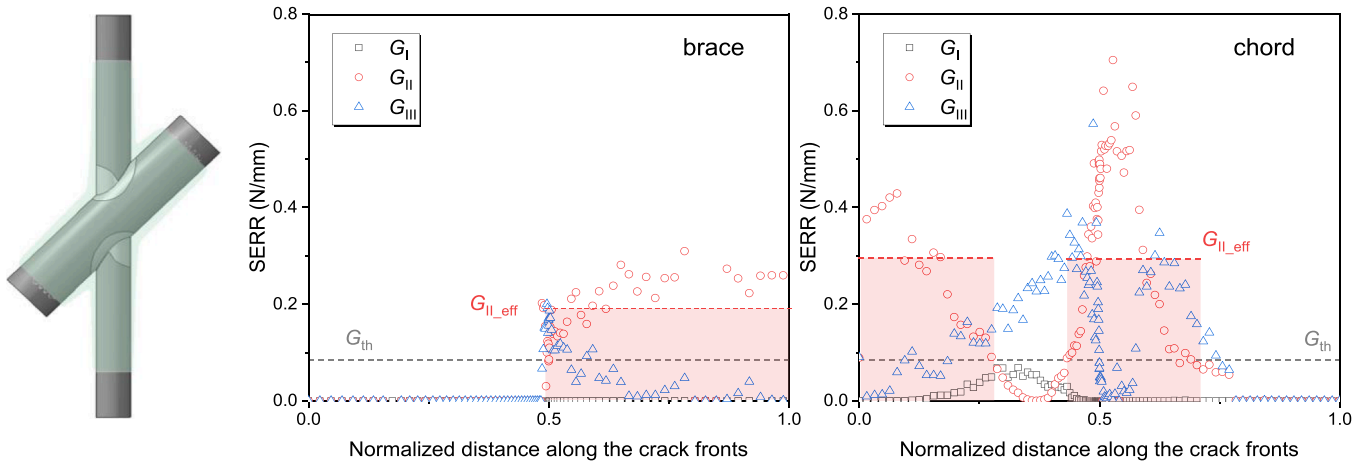
Fig. 32. Typical crack pattern and SERR distribution on the crack tip of brace and chord for upscaled joints.
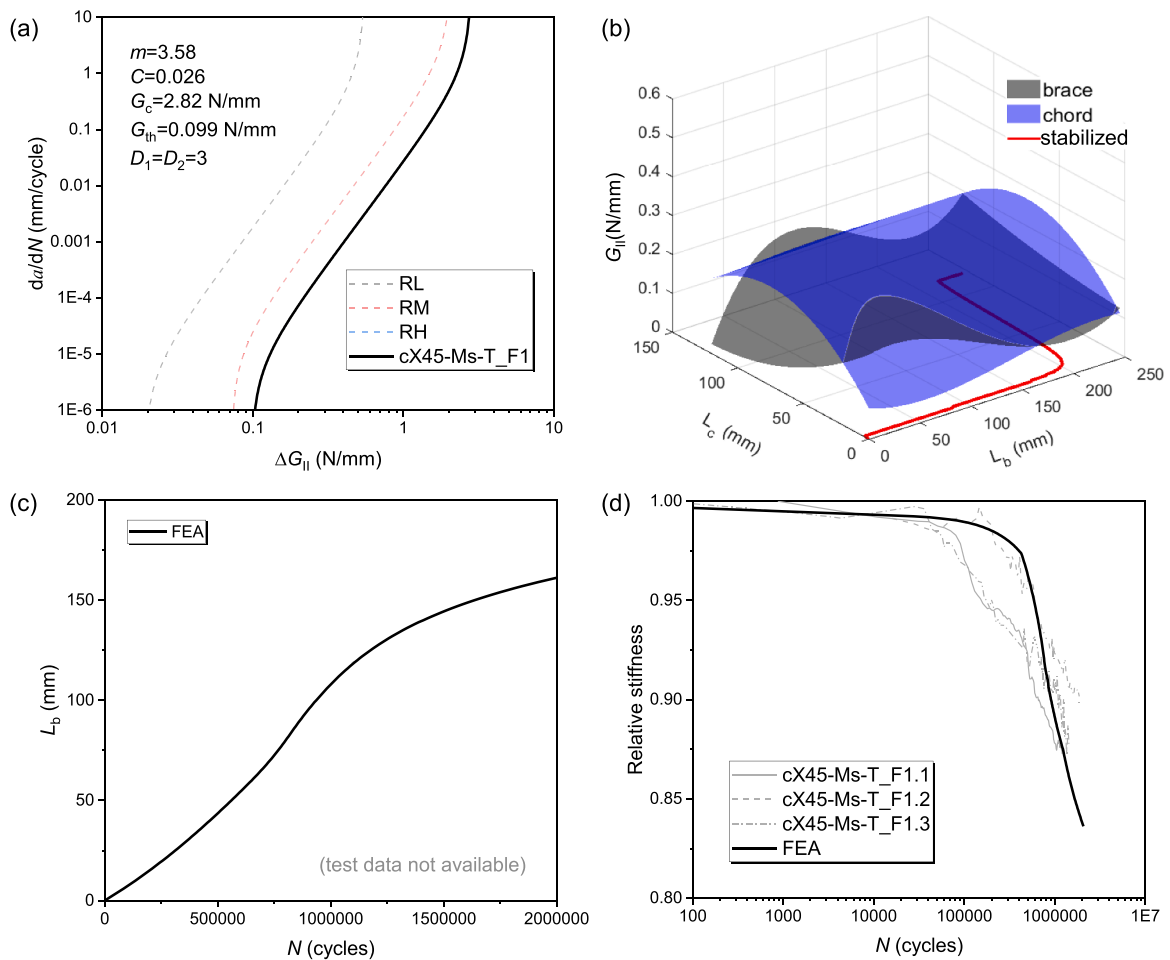

Fig. 33. Modelling results for upscaled joints (a) interpolated FCG curve; (b) SERR surfaces; (c) crack growth; (d) stiffness degradation.

shows that the relative error of the two results is within a reasonable range, with the coefficient of determination, R^2, being 0.79.

Calibrated based on small scale joint tests, the proposed FE modelling methodology is successfully validated by the upscaled joint test, demonstrating its capacity to predict fatigue debonding behaviour in a complex bi-material interface, regardless of joint scale.

6. Conclusions

This paper establishes a numerical methodology to simulate the fatigue debonding behaviour at the bi-material interface with a complex geometry, taking the wrapped composite joint as an example. The FE model is built and preliminarily validated against the static test results in terms of force-displacement responses and surface strains on the composite wrap. The stationary crack growth method is proposed for predicting fatigue debonding behaviour, and calibrated based on tests of
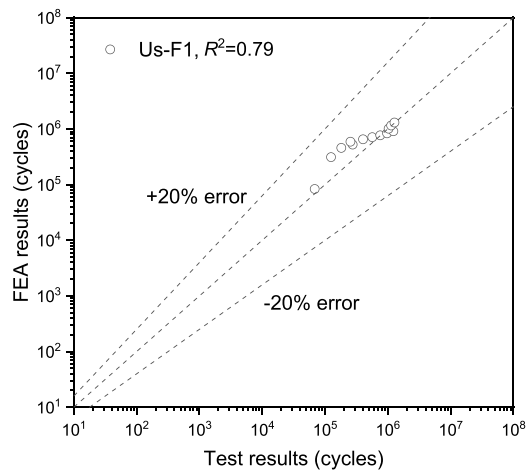
Fig. 34. Comparison of fatigue lives under different failure criteria between test and FEA results for upscale joints.

small scale joints with different roughness subject to different load levels. Key modelling parameters are calibrated through a sensitivity analysis. The calibrated model is finally validated against test results on upscaled joints. The following conclusions can be drawn from this paper:

- The FE model where VCCT in combination with friction is utilized to simulate the fracture behaviour at the composite-to-steel interface can well reproduce the force-displacement responses and surface strain distributions on the composite wrap obtained from the static tests. The fracture toughness is calibrated based on the modelling results as to be 1.02 N/mm for mode I and 1.34 N/mm for mode II.
- The fatigue debonding behaviour is simulated by the proposed stationary crack growth method, where the debonding crack patterns are assumed to be the same as those in the static debonding process. The SERR values are extracted at the crack tips and the number of cycles needed for crack growth is calculated based on the FCG properties in an algorithm with an iterative procedure, where the interaction between crack growth on the chord and braces can be considered. The calibrated FE model can well replicate the crack growth and stiffness degradation of the small scale joint with different surface roughness subject to different load levels, with the prediction error of stiffness-controlled fatigue live within 30 % in the linear scale and within 10 % in the logarithmic scale.
- Key modelling parameters are calibrated through a sensitivity analysis by comparing the modelling results with test results of small scale joints. It was found out that the prediction results are most sensitive to the curvature exponent, D, and the threshold, G_{th}, of the total life FCG curves. The curvature exponent is calibrated to be 3 and the SERR threshold to be 3 % of the fracture toughness.
- The proposed FE modelling methodology, primarily calibrated on small scale joint tests, is successfully validated by comparison of the FE model and the test results on the upscaled joint, demonstrating its capacity to predict fatigue debonding behaviour in a complex bi-material interface regardless of joint scale

CRediT authorship contribution statement

Sigurdur Egilsson: Writing – review & editing, Methodology, Investigation. **Weikang Feng:** Writing – original draft, Visualization, Methodology, Investigation, Formal analysis, Data curation. **Mees Wolters:** Writing – review & editing, Methodology, Investigation. **Marko Pavlovic:** Writing – review & editing, Supervision, Project administration, Methodology, Funding acquisition, Conceptualization.

Declaration of Competing Interest

The authors declare that they have no known competing financial interests or personal relationships that could have appeared to influence the work reported in this paper.

Data availability

Data will be made available on request.

References

[1] Borrie D, Al-saadi S, Zhao XL, Raman Singh, Bai RK. Y. Bonded cfrp/steel systems, remedies of bond degradation and behaviour of CFRP repaired steel: an overview. Polymers 2021;13. https://doi.org/10.3390/POLYM13091533.

[2] Zhao XL, Zhang L. State-of-the-art review on FRP strengthened steel structures. Eng Struct 2007;29:1808–23. https://doi.org/10.1016/j.engstruct.2006.10.006.

[3] Feng W, Pavlovic M. Fatigue behaviour of non-welded wrapped composite joints for steel hollow sections in axial load experiments. Eng Struct 2021;249:113369. https://doi.org/10.1016/J.ENGSTRUCT.2021.113369.

[4] He P, Pavlovic M. Failure modes of bonded wrapped composite joints for steel circular hollow sections in ultimate load experiments. Eng Struct 2022;254: 113799. https://doi.org/10.1016/j.engstruct.2021.113799.

[5] Pavlovic M, Bogers P, Veljkovic M. Method for making a virgin joint between two separate structural hollow sections, and such a virgin joint 2021;17(052):303.

[6] Feng W, He P, Pavlovic M. Combined DIC and FEA method for analysing debonding crack propagation in fatigue experiments on wrapped composite joints. Compos Struct 2022:115977. https://doi.org/10.1016/J.COMPSTRUCT.2022.115977.

[7] Pascoe JA, Alderliesten RC, Benedictus R. Methods for the prediction of fatigue delamination growth in composites and adhesive bonds - a critical review. Eng Fract Mech 2013;112–113:72–96. https://doi.org/10.1016/j.engfracmech.2013.10.003.

[8] Liniecki A, Hsu TR, Li W. Fatigue strength of adhesive bonded aluminum joints. J Test Eval 1995;23:453–68. https://doi.org/10.1520/JTE11435J.

[9] Renton JW, Vinson JR. On the behavior of bonded joints in composite material structures. Eng Fract Mech 1975;7:41–60.

[10] Ratwani MM, Kan HP. Compression fatigue analysis of fiber composites. J Aircr 1981;18:458–62.

[11] Poursartip A, Chinatambi N. Fatigue damage development in notched (02/±45) s laminates. Compos Mater Fatigue Fract 1989;2:45–65.

[12] Hallett SR, Harper PW. Modelling delamination with cohesive interface elements. Numer. Model. Fail. Adv. Compos. Mater. Elsevier Ltd,; 2015. p. 55–72. https://doi.org/10.1016/B978-0-08-100332-9.00002-5.

[13] Harper PW, Hallett SR. A fatigue degradation law for cohesive interface elements – development and application to composite materials. Int J Fatigue 2010;32: 1774–87. https://doi.org/10.1016/j.ijfatigue.2010.04.006.

[14] Fernández MV, de Moura MFSF, da Silva LFM, Marques AT. Composite bonded joints under mode I fatigue loading. Int J Adhes Adhes 2011;31:280–5. https://doi.org/10.1016/j.ijadhadh.2010.10.003.

[15] Rocha AVM, Akhavan-Safar A, Carbas R, Marques EAS, Goyal R, El-zein M, et al. Numerical analysis of mixed-mode fatigue crack growth of adhesive joints using CZM. Theor Appl Fract Mech 2020;106:102493. https://doi.org/10.1016/J.TAFMEC.2020.102493.

[16] Choi Y-H, Kim H-G. Development of a cohesive zone model for fatigue crack growth. Multiscale Sci Eng 2020;2:42–53. https://doi.org/10.1007/s42493-020-00034-5.

[17] Martin R.H., Murri G.B. Characterization of mode I and mode II delamination growth and thresholds in AS4/PEEK composites; 1990.

[18] Krueger R. The virtual crack closure technique for modeling interlaminar failure and delamination in advanced composite materials. Numer. Model. Fail. Adv. Compos. Mater. Elsevier Ltd.; 2015. p. 3–53. https://doi.org/10.1016/B978-0-08-100332-9.00001-3.

[19] Rans C, Alderliesten R, Benedictus R. Misinterpreting the results: how similitude can improve our understanding of fatigue delamination growth. Compos Sci Technol 2011;71:230–8. https://doi.org/10.1016/j.compscitech.2010.11.010.

[20] Quaresimin M, Ricotta M. Stress intensity factors and strain energy release rates in single lap bonded joints in composite materials. Compos Sci Technol 2006;66: 647–56. https://doi.org/10.1016/J.COMPSCITECH.2005.07.036.

[21] Quaresimin M, Ricotta M. Life prediction of bonded joints in composite materials. Int J Fatigue 2006;28:1166–76. https://doi.org/10.1016/j.ijfatigue.2006.02.005.

[22] Abaqus Unified FEA - SIMULIA™ by Dassault Systèmes® n.d. Available from: https://www.3ds.com/products-services/simulia/products/abaqus/. [Accessed 12 May 2022].

[23] Pirondi A, Giuliese G, Moroni F, Bernasconi A, Jamil A. Comparative study of cohesive zone and virtual crack closure techniques for three-dimensional fatigue debonding. J Adhes 2014;90:457–81. https://doi.org/10.1080/00218464.2013.859616.

[24] Martulli LM, Bernasconi A. An efficient and versatile use of the VCCT for composites delamination growth under fatigue loadings in 3D numerical analysis: the Sequential Static Fatigue algorithm. Int J Fatigue 2023;170:107493. https://doi.org/10.1016/J.IJFATIGUE.2022.107493.

[25] Russo A, Riccio A, Sellitto A. A robust cumulative damage approach for the simulation of delamination under cyclic loading conditions. Compos Struct 2022; 281:114998. https://doi.org/10.1016/j.compstruct.2021.114998.

[26] Russo A, Palumbo C, Sellitto A, Riccio A. The peculiar SMart-Time XB approach for delamination growth prediction and its evolution towards fatigue investigations. Int J Solids Struct 2024;291:112681. https://doi.org/10.1016/j.ijsolstr.2024.112681.

[27] Feng W, Arouche MM, Pavlovic M. Influence of surface roughness on the mode II fracture toughness and fatigue resistance of bonded composite-to-steel joints. Constr Build Mater 2024;411:134358. https://doi.org/10.1016/j.conbuildmat.2023.134358.

[28] Landry B, Laplante G, Leblanc LR. Environmental effects on mode II fatigue delamination growth in an aerospace grade carbon/epoxy composite. Compos Part A Appl Sci Manuf 2012;43:475–85. https://doi.org/10.1016/j.compositesa.2011.11.015.

[29] Shahverdi M, Vassilopoulos AP, Keller T. A total fatigue life model for the prediction of the R-ratio effects on fatigue crack growth of adhesively-bonded pultruded GFRP DCB joints. Compos Part A Appl Sci Manuf 2012;43:1783–90. https://doi.org/10.1016/j.compositesa.2012.05.004.

[30] Matsubara G, Ono H, Tanaka K. Mode II fatigue crack growth from delamination in unidirectional tape and satin-woven fabric laminates of high strength GFRP. Int J Fatigue 2006;28:1177–86. https://doi.org/10.1016/j.ijfatigue.2006.02.006.

[31] Hojo M, Ando T, Tanaka M, Adachi T, Ochiai S, Endo Y. Modes I and II interlaminar fracture toughness and fatigue delamination of CF/epoxy laminates with self-same epoxy interleaf. Int J Fatigue 2006;28:1154–65. https://doi.org/10.1016/J.IJFATIGUE.2006.02.004.

[32] Asp LE, Sjögren A, Greenhalgh ES. Delamination growth and thresholds in a carbon/epoxy composite under fatigue loading. J Compos Technol Res 2001;23: 55–68. https://doi.org/10.1520/ctr10914j.

[33] Feng W, He P, Pavlovic M. Combined DIC and FEA method for analysing debonding crack propagation in fatigue experiments on wrapped composite joints. Compos Struct 2022;297:115977. https://doi.org/10.1016/J.COMPSTRUCT.2022.115977.

[34] He P. Debonding resistance of CHS wrapped composite X-joints. Delft University of Technology; 2023. Available from: https://doi.org/https://doi.org/10.4233/uuid:3ad94ee9–07fd-47f9-a766–843a91830534.

[35] Benzeggagh ML, Kenane M. Measurement of mixed-mode delamination fracture toughness of unidirectional glass/epoxy composites with mixed-mode bending apparatus. Compos Sci Technol 1996;56:439–49. https://doi.org/10.1016/0266-3538(96)00005-X.

[36] Feng W, Pavlovic M, Koetsier M, Veljkovic M. Interfacial fatigue debonding retardation in wrapped composite joints: experimental and numerical study. Compos Struct 2023;319:117146. https://doi.org/10.1016/j.compstruct.2023.117146.

[37] Takeda T, Miura M, Shindo Y, Narita F. Fatigue delamination growth in woven glass / epoxy composite laminates under mixed-mode II / III loading conditions at cryogenic temperatures. Cryogenics 2013;58:55–61. https://doi.org/10.1016/j.cryogenics.2013.10.001.

[38] Miura M, Shindo Y, Narita F, Watanabe S, Suzuki M. Mode III fatigue delamination growth of glass fiber reinforced polymer woven laminates at cryogenic temperatures. Cryogenics 2009;49:407–12. https://doi.org/10.1016/J.CRYOGENICS.2009.05.004.

[39] Egilsson S. Fatigue of wrapped composite joints fatigue of wrapped composite joints. Delft University of Technology; 2023.

[40] Feng W. Fatigue debonding resistance of wrapped composite X-joints. Delft University of Technology; 2024. Available from: https://doi.org/https://doi.org/10.4233/uuid:609be108–6fd4–4a24–8677-7d76bbec3515.